

BACHELOR'S THESIS

**Electronic and topological properties of
graphene nanoribbons**

Niclas Heinsdorf

Institut für Theoretische Physik
Johann Wolfgang Goethe-Universität
Frankfurt am Main

August 2018

1st Supervisor: Prof. Dr. Roser Valentí
2nd Supervisor: Prof. Dr. Eberhard Engel

Contents

1	Motivation and Outline	5
2	Topological band theory	7
2.1	Gauß-Bonnet theorem	7
2.2	Berry phase	8
2.3	Chern number	10
2.3.1	Chern number of time-reversal-invariant systems	10
3	Quantum Hall effect	13
3.1	Classical Hall effect	13
3.1.1	Classical picture	14
3.1.2	Drude Model	14
3.2	Quantization of Hall conductivity	15
3.2.1	Experimental results	15
3.2.2	Landau levels	16
3.3	Classical edge states	18
3.4	Kubo Formula	19
3.5	Hall conductivity as a Chern number	21
3.6	Topological edge states	23
4	Density functional theory	25
4.1	Hohenberg-Kohn Theorems	25
4.1.1	Proof of theorem 1	26
4.1.2	Proof of theorem 2	27
4.2	Kohn-Sham ansatz	27
4.3	Perdew-Burke-Ernzerhof generalized-gradient approximation	30
4.4	WIEN2k	32
5	Graphene	33
5.1	Electronic structure of graphene	33
5.1.1	Tight-binding	33
5.1.2	Massless Dirac Fermions	35
5.1.3	DFT calculations for graphene	36
5.2	Symmetries	36
5.2.1	Inversion symmetry	37
5.2.2	Time-reversal symmetry	37
5.2.3	Symmetry protection of the Dirac points	37
5.3	Topological properties	38
5.3.1	Berry phase of graphene	38
5.3.2	Breaking inversion symmetry	40

5.3.3	Breaking time-reversal symmetry and the Haldane model	40
6	\mathbb{Z}_2 invariant	43
7	Su-Schrieffer-Heeger model	47
7.1	Tight-binding of polyacetylene	47
7.2	Topological properties of polyacetylene	49
7.3	SSH model for AGNR composites	50
8	Graphene nanoribbons	53
8.1	Different forms of graphene nanoribbons	53
8.2	Tight-binding of AGNR of any width	53
8.3	DFT calculation for AGNR	58
8.4	AGNR composites	60
8.4.1	3/5/3 AGNR composites	61
9	Discussion and Outlook	67
	Bibliography	71

1 Motivation and Outline

"Point set topology is a disease from which the human race will soon recover."

-Henri Poincaré, 1908 [1]

Although the Poincaré conjecture was solved in November 2002 by Grigori Perelman, the conjecture cited above has not come true yet. Rather the opposite is the case. Topology has become a thriving field of study for many physicists and in 2016 the Nobel Prize in physics was awarded to D. J. Thouless, F. D. M. Haldane and J. M. Kosterlitz "for theoretical discoveries of topological phase transitions and topological phases of matter" [2].

In 1982 Thouless, Kohmoto, Nightingale and den Nijs managed to link the quantized Hall conductance to the hitherto purely mathematical concept of Chern classes [3]. They showed that where the classical theory of phase transitions failed, topological methods are capable of describing these exotic phases.

The topological order of these special systems gives rise to edge states localized at the boundary between a topological and a trivial material. For us, the coupling of these edge or rather interface states with each other is of particular interest.

This thesis is structured as follows: First, an introduction to the theoretical framework underlying topological band theory is given. To this end it is shown how insulators are classified by examining the geometry of their band structure using the concept of the Berry phase.

In chapter 3 this approach in combination with linear response theory is employed to explain the integer quantum Hall effect. The biggest part of these two chapters is taken from the flip lecture I gave on this topic earlier this semester [4].

Afterwards, the notion of density functional theory (DFT) is established as it is our method of choice for gaining insight into the electronic structure of condensed matter. This section is then concluded by presenting WIEN2k, which is the program package that has been used to do the DFT calculations.

Chapter 5 is wholly dedicated to the analysis of graphene. We investigate its electronic structure by analytical and numerical means, explore its symmetries and the consequences of breaking them and derive the Berry phase around graphene's Dirac points.

To dispense the impression that in the end graphene does not exhibit interesting topological properties at all, the \mathbb{Z}_2 invariant is introduced (Ch.6). By cutting our previously infinitely extended sheet of graphene into thin stripes in chapter 8, which are called graphene nanoribbons (GNR), we learn how this topological invariant changes depending on the width, shape and termination of these new quasi-1D systems using the results of [5].

Subsequently, chapter 7 presents the Su-Schrieffer-Heeger (SSH) for the electronic transport in long chains of polyacetylene and shows how this well-known model links to the

dispersion of our bands of interest.

Finally, different GNR are put together in order to reproduce the interesting effects of [6] and to verify the validity of their interpretation, namely the appearance of new, "topologically induced" bands in the energy spectrum due to the coupling of interface states. As our computational power is limited, we try to keep the composite structures as small as possible while still recreating the desired effect.

This thesis is then concluded in chapter 9 by summarizing the results and giving an outlook on how they can be applied.

2 Topological band theory

Despite the fact that electronic band theory exists for almost a century now, it was recognized only recently that this picture is not sufficient to describe all systems. Taking into consideration the geometry of the band space, one can find new and exciting phases where the line between insulator and metal starts to get blurred, as these materials are insulators in their bulk, but conduct electricity at their boundaries. To provide a foundation for understanding this phenomenon, the concept of the Berry phase is introduced, giving us the tool for classifying differently ordered phases by linking them to a topological invariant. We start off by reminding ourselves of a topological concept from geometry we are already familiar with.

2.1 Gauß-Bonnet theorem



Fig. 2.1: A sphere (a) with genus $g = 0$ and a torus (b) with genus $g = 1$. As they have different genera they are not connected by any homeomorphism.

The Gauß-Bonnet theorem associates the geometry of a surface to its topology by establishing a relation between its curvature \mathcal{K} with its genus g (or more exact, its Euler characteristic). The genus g is a topological invariant, meaning its value stays invariant under homeomorphisms, which are continuous functions that have a continuous inverse function. Let M be a compact two-dimensional Riemannian manifold without boundary and with a compact, orientable surface and let \mathcal{K} be the Gaussian curvature of M and dA the element of area, then

$$\int_M \mathcal{K} dA = 2\pi(2 - 2g). \quad (2.1)$$

The genus g is basically the number of holes in the object. A sphere, which has a Gaussian curvature \mathcal{K} of 1 in each point, has therefore a genus of $g = 0$, whereas a torus has a genus of $g = 1$ (see Fig.2.1). Notice that the genus g can only take integer values.

2.2 Berry phase

Next, we will extrapolate the concept of the previous section to parameter space. Our goal is to find a topological invariant that classifies band structures that are not adiabatically connected, and thus stays invariant under continuous transformations.

Accordingly, let us consider a parameter dependent Hamiltonian $H(\mathbf{R}(t))$ where \mathbf{R} is a n -dimensional, time dependent vector, which is moving on a closed loop \mathcal{C} in parameter space and $|n(\mathbf{R}(t))\rangle$ as the normalized instantaneous eigenstate of $H(\mathbf{R}(t))$ with

$$H(\mathbf{R}(t)) |n(\mathbf{R}(t))\rangle = E_n(\mathbf{R}(t)) |n(\mathbf{R}(t))\rangle. \quad (2.2)$$

This equation determines the eigenstate $|n(\mathbf{R}(t))\rangle$ only up to a phase and we know per adiabatic theorem that for slow variation of \mathbf{R} the system remains in its eigenstate [8]. We will now consider the phase $\theta(t)$ of the state $|\psi(t)\rangle = e^{-i\theta(t)} |n(\mathbf{R}(t))\rangle$ during an adiabatic evolution along the loop \mathcal{C} . The time evolution of the system is given by

$$H(\mathbf{R}(t)) |\psi(t)\rangle = i\hbar \frac{d}{dt} |\psi(t)\rangle \quad (2.3)$$

which yields

$$E_n(\mathbf{R}(t)) |n(\mathbf{R}(t))\rangle = \hbar \left(\frac{d}{dt} \theta(t) \right) |n(\mathbf{R}(t))\rangle + i\hbar \frac{d}{dt} |n(\mathbf{R}(t))\rangle. \quad (2.4)$$

Taking the dot product with $\langle n(\mathbf{R}(t))|$ and integrating, we obtain

$$\theta(t) = \frac{1}{\hbar} \int_0^t E_n(\mathbf{R}(t')) dt' - i \int_0^t \langle n(\mathbf{R}(t'))| \frac{d}{dt'} |n(\mathbf{R}(t'))\rangle dt'. \quad (2.5)$$

The first part is the dynamical phase factor, which we already know, whereas the negative of the second term is the so-called Berry or geometrical phase γ_n

$$\gamma_n = i \int_0^t \langle n(\mathbf{R}(t'))| \frac{d}{dt'} |n(\mathbf{R}(t'))\rangle dt'. \quad (2.6)$$

The Berry phase is the most important concept in topological band theory, although it was not even related specifically to Bloch bands originally. Berry was rather interested in the idea that the wave functions of particles in a slowly varying field could, in principle, be modified by something other than just the dynamical phase. Only later it has been realized that this concept can be applied to the Bloch-periodic system in a crystal, where the parameter $\mathbf{R}(t)$ corresponds to the crystal momentum \mathbf{k} . The loop in k -space can be considered as closed due to the periodicity of the Brillouin zone.

As the eigenstates $|n\rangle$ depend on \mathbf{R} , we can just as well parameterize the evolution of our eigenstates with respect to \mathbf{R} and thereby get rid of the explicit time dependence.

$$\gamma_n = i \int_0^t \langle n(\mathbf{R}(t'))| \nabla_{\mathbf{R}} |n(\mathbf{R}(t'))\rangle \frac{d\mathbf{R}}{dt'} dt' = i \int_{\mathcal{C}} \langle n(\mathbf{R})| \nabla_{\mathbf{R}} |n(\mathbf{R})\rangle d\mathbf{R} \quad (2.7)$$

Note that the time dependence of \mathbf{R} has been dropped and that $\nabla_{\mathbf{R}}$ is a n -dimensional vector defined as $\nabla_{\mathbf{R}} = (\frac{\partial}{\partial R_1}, \frac{\partial}{\partial R_2} \dots \frac{\partial}{\partial R_n})^\top$.

In analogy to electromagnetism let us define a vector potential \mathcal{A}_n , called the Berry connection:

$$\mathcal{A}_n(\mathbf{R}) = i \langle n(\mathbf{R}) | \nabla_{\mathbf{R}} | n(\mathbf{R}) \rangle \quad (2.8)$$

$$\Rightarrow \quad \gamma_n = \int_{\mathcal{C}} d\mathbf{R} \mathcal{A}_n(\mathbf{R}) \quad (2.9)$$

One might be tempted to think that one should always be able to find a gauge where the Berry phase γ_n is canceled. However, this is not true. From the beginning of this section we assumed that we are moving on a closed path \mathcal{C} in parameter space. In order to understand why this postulate was even necessary, let us examine the behavior of the Berry connection \mathcal{A}_n under gauge transformations.

Under a $U(1)$ gauge transformation $|n(\mathbf{R})\rangle \rightarrow e^{i\Lambda(\mathbf{R})} |n(\mathbf{R})\rangle$ the vector potential \mathcal{A}_n transforms in the usual way

$$\mathcal{A}_n(\mathbf{R}) \rightarrow \mathcal{A}_n(\mathbf{R}) - \nabla_{\mathbf{R}}\Lambda(\mathbf{R}) \quad (2.10)$$

with $\Lambda(\mathbf{R})$ as any smooth and single-valued function. Moving on a closed loop means that we will return to our initial parameter configuration $\mathbf{R}(0)$ after a period T . Therefore, $\mathbf{R}(0) = \mathbf{R}(T)$. Because we chose our eigenstate basis $|n(\mathbf{R})\rangle$ to be single-valued, $|n(\mathbf{0})\rangle = |n(\mathbf{T})\rangle$ must hold as well. As gauge transformations must maintain the aforementioned properties, we get

$$\begin{aligned} e^{i\Lambda(\mathbf{R}(0))} |n(\mathbf{R}(0))\rangle &= e^{i\Lambda(\mathbf{R}(T))} |n(\mathbf{R}(T))\rangle \\ \Leftrightarrow e^{i\Lambda(\mathbf{R}(0))} |n(\mathbf{R}(0))\rangle &= e^{i\Lambda(\mathbf{R}(T))} |n(\mathbf{R}(0))\rangle \\ \Leftrightarrow \Lambda(\mathbf{R}(T)) - \Lambda(\mathbf{R}(0)) &= 2\pi n \quad \text{with } n \in \mathbb{Z} \end{aligned} \quad (2.11)$$

As such, the Berry phase γ_n is a gauge invariant quantity and can not be cancelled by a choice of gauge, as long as \mathbf{R} is varied on a closed path \mathcal{C} . If that is the case, we can apply Stokes' theorem to (2.9):

$$\gamma_n = \int_{\mathcal{C}} d\mathbf{R} \mathcal{A}_n(\mathbf{R}) = \int_{\mathcal{S}} d\mathbf{S} \nabla_{\mathbf{R}} \times \mathcal{A}_n \quad (2.12)$$

where \mathcal{S} is the surface enclosed by the loop \mathcal{C} and $d\mathbf{S}$ the element of area. The integrand of this equation is called the Berry curvature \mathcal{F}_n and is the analog to the Gaussian curvature \mathcal{K} :

$$\mathcal{F}_n = \nabla_{\mathbf{R}} \times \mathcal{A}_n \quad (2.13)$$

Due to its resemblance to the well-known expression from electrodynamics, the Berry curvature has often been referred to as the magnetic field in parameter space.

2.3 Chern number

Now, as we have worked out an expression for the curvature of parameter space, we are ready to define a topological invariant in analogy to the Gauß-Bonnet theorem presented in section 2.1. Just as the genus of a surface, it only takes integer values and stays invariant under any continuous transformation or rather conveyance to an adiabatically connected system.

In mathematics, the Chern classes are used to test the equivalence of complex vector bundles and were introduced in 1946 by Shiing-Shen Chern [9].

For us, the Chern number of the n^{th} band C_n is proportional to the surface integral of the Berry curvature \mathcal{F}_n over \mathcal{S} , which is the surface enclosed by loop \mathcal{C} . The total Chern number C is just the sum of all C_n and is then given by

$$C = \frac{1}{2\pi} \sum_n \int_{\mathcal{S}} \mathcal{F}_n. \quad (2.14)$$

In a crystal we identify the parameter \mathbf{R} with the crystal momentum k . Thus, \mathcal{S} is just the area of the first Brillouin zone. As we are only interested in the geometry of the bands that are actually occupied, the sum only runs over the filled bands.

In the next chapter we will show that the Chern number of a two-dimensional system can be related to the Hall conductance.

2.3.1 Chern number of time-reversal-invariant systems

Although topological phases of matter are not tied to a broken discrete and continuous symmetry, they can be protected by one. Let us examine what a system with time-reversal symmetry implies for the Chern number.

Time reversal is a discrete symmetry that flips the direction of time.

$$T : t \rightarrow -t \quad (2.15)$$

A system is called time-invariant if the particles of that system retraced their motion upon reversal of time.

T is an operator that leaves the position operators unchanged, but acts upon the momenta, as they are time derivatives of the position operators (which are invariant under time reversal). Furthermore, T is anti-unitary which means it is the product of a unitary matrix U and the complex conjugation operator K . For spinless particles this unitary matrix is just the identity $U = \mathbf{1}$.

Having identified $T = K$ (for spinless particles), we can determine our system's behavior under time reversal as

$$TH(\mathbf{q})T^{-1} = H(-\mathbf{q}) \quad (2.16)$$

where we used that K commutes with the creation and annihilation operators $a(\mathbf{R})$ and $b(\mathbf{R})$.

Applying T to the Berry curvature $\mathcal{F}_{n,i}$, we get

$$\begin{aligned}
T\mathcal{F}_{n,i}(\mathbf{R}) &= T(\varepsilon_{ijk} \partial_{\mathbf{R}_j} \mathcal{A}_k) \\
&= i\varepsilon_{ijk} \langle \partial_{\mathbf{R}_j} Tn(\mathbf{R}) | \partial_{\mathbf{R}_k} Tn(\mathbf{R}) \rangle \\
&= i\varepsilon_{ijk} \langle \partial_{\mathbf{R}_k} Tn(-\mathbf{R}) | \partial_{\mathbf{R}_j} Tn(-\mathbf{R}) \rangle \\
&= -i\varepsilon_{ikj} \langle \partial_{\mathbf{R}_k} Tn(-\mathbf{R}) | \partial_{\mathbf{R}_j} Tn(-\mathbf{R}) \rangle \\
&= -\mathcal{F}_{n,i}(-\mathbf{R})
\end{aligned} \tag{2.17}$$

The anti-symmetry of the Levi-Civita tensor has been used. Requiring that our system is time-reversal invariant, such that $T\mathcal{F}_{n,i}(\mathbf{R}) = \mathcal{F}_{n,i}(\mathbf{R})$, it follows that the Berry curvature must be an odd function of \mathbf{R} :

$$\mathcal{F}_{n,i}(-\mathbf{R}) = -\mathcal{F}_{n,i}(\mathbf{R}) \tag{2.18}$$

Using this result on equation 2.14, we obtain

$$\begin{aligned}
T C_n &= \frac{1}{2\pi} \int_S T \mathcal{F}_n(\mathbf{R}) = -\frac{1}{2\pi} \int_S \mathcal{F}_n(-\mathbf{R}) = -C_n \\
\Rightarrow C_n &= 0
\end{aligned} \tag{2.19}$$

Hence, we have proved that only systems with broken time-reversal symmetry can exhibit a non-zero Chern number.

3 Quantum Hall effect

The abstract concepts of the preceding chapter are now applied to a real system. The discovery that the quantization of the Hall conductance can be explained by means of topology made a strong impact and as a consequence many physicists turned their attention to this field of study.

After a short comparison of the results that would have been expected classically with the actual results measured by Klaus von Klitzing in 1980 [10], we show that the Hall conductance is proportional to the Chern number. This relation is sometimes called Thouless, Kohmoto, Nightingale, den Nijs (TKNN) invariant [3].

3.1 Classical Hall effect

The classical Hall effect, or sometimes ordinary Hall effect, was discovered by Edwin Hall in 1879 [11].

Consider a quasi-2D conductor, e.g. a very thin sheet of metal. If a constant current of electrons \mathbf{I} is made to flow into one direction and the sample is subjected to a perpendicular magnetic field \mathbf{B} , a transversal difference in current U_H is produced. This current is the Hall conductance, which is proportional to the magnetic field \mathbf{B} and the current \mathbf{I} with the Hall constant R_H being the proportionality constant.

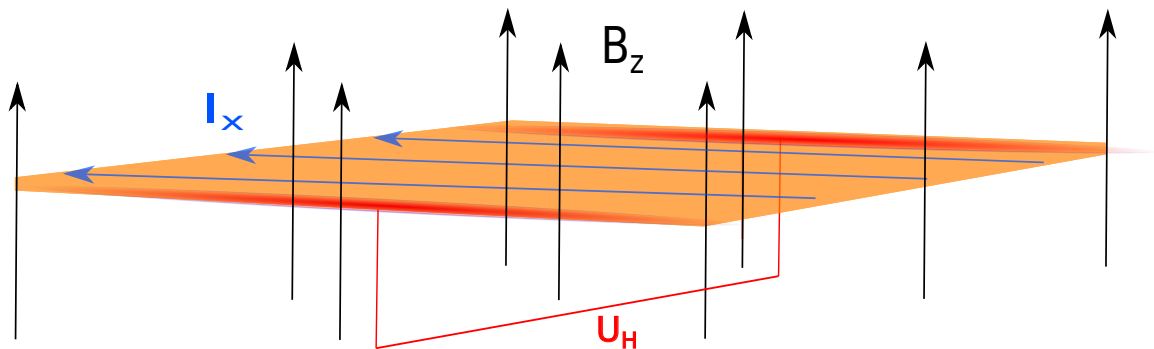


Fig. 3.1: The classical Hall effect: As the electrons are restricted to move only in the xy -plane (orange), the magnetic field B in the z -direction (black) in combination with the electrons' direction of movement I in x -direction (blue) results in a potential difference on the y -boundaries of the sample (red), which is called the Hall conductance U_H .

3.1.1 Classical picture

The equations of motions for a charged particle in a magnetic field \mathbf{B} with charge $q = -e$ and mass m_e are

$$m_e \ddot{\mathbf{r}} = -e \dot{\mathbf{r}} \times \mathbf{B}. \quad (3.1)$$

In our case the magnetic field points along the z-direction and the current is restricted to the transverse plane, so that $\mathbf{B} = (0, 0, B)^\top$ and $\dot{\mathbf{r}} = (\dot{x}, \dot{y}, 0)^\top$. Computing the cross product we obtain two coupled differential equations:

$$\begin{aligned} m_e \ddot{x} &= -eB\dot{y} \\ m_e \ddot{y} &= eB\dot{x} \end{aligned} \quad (3.2)$$

Their general solutions read

$$\begin{aligned} x(t) &= x_0 - R \sin(\omega_0 t + \varphi_0) \\ y(t) &= y_0 + R \cos(\omega_0 t + \varphi_0) \end{aligned} \quad (3.3)$$

We can easily see that the electrons move on circles with a frequency ω_0 that is also called cyclotron frequency and is given by

$$\omega_0 = \frac{eB}{m}. \quad (3.4)$$

The radius R , as well as their phase φ_0 and their initial positions x_0, y_0 , are determined by the initial conditions.

3.1.2 Drude Model

Now, we take into account an electric field \mathbf{E} that will result in a current of particles and a linear scattering term which models the effect of electrons bouncing off impurities, other electrons or the lattice. The resulting equations of motion are given by

$$m_e \ddot{\mathbf{r}} = -e \dot{\mathbf{r}} \times \mathbf{B} - e\mathbf{E} - \frac{m}{\tau} \dot{\mathbf{r}}. \quad (3.5)$$

The coefficient τ in the friction term is the scattering time. These equations are called the Drude model and restricting oneself to its equilibrium solutions one can obtain Ohm's law

$$\mathbf{J} = \sigma \mathbf{E} \quad (3.6)$$

with \mathbf{J} being the the current density and σ is the conductivity matrix. As we know, the current density is given by

$$\mathbf{J} = -ne \dot{\mathbf{r}} \quad (3.7)$$

where n is the charge density. It can be shown that the following expression holds

$$\sigma = \frac{\sigma_0}{1 + \omega_0^2 \tau^2} \begin{pmatrix} 1 & -\omega_0 \tau \\ \omega_0 \tau & 1 \end{pmatrix} \quad \text{with} \quad \sigma_0 = \frac{ne^2}{m_e} \tau. \quad (3.8)$$

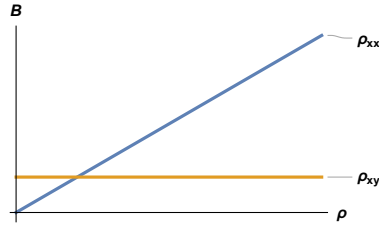


Fig. 3.2: Resistivity in dependence of the magnetic field. ρ_{xx} (orange) depicts the longitudinal part of the resistivity, which is parallel to the current \mathbf{J} , whereas ρ_{xy} (blue) shows the transverse resistivity.

σ_0 describes the conductivity in the absence of a magnetic field. The resistivity ρ is defined as the inverse of the conductivity σ , so taking into account (3.8) we get

$$\rho = \sigma^{-1} = \frac{m_e}{ne^2\tau} \begin{pmatrix} 1 & \omega_0\tau \\ -\omega_0\tau & 1 \end{pmatrix}. \quad (3.9)$$

Thus, the longitudinal and transverse components of the resistivity should amount to

$$\rho_{xx} = \frac{m}{ne^2\tau} \quad \text{and} \quad \rho_{xy} = \frac{B}{ne}. \quad (3.10)$$

So considering the classical picture, we are expecting a constant longitudinal resistivity ρ_{xx} and a linearly increasing transverse resistivity ρ_{xy} with an increasing magnetic field B (see Fig.3.2).

3.2 Quantization of Hall conductivity

3.2.1 Experimental results

We have set our expectations on how the Hall conductivity should behave under a strong magnetic field, but the precedent section would not have been named "classical" Hall effect if there were not any caveats to our previous discussion.

It was Klaus von Klitzing who received the Nobel prize in 1985 for his discovery that the classical model does not sufficiently describe the behavior of the resistivity for strong magnetic fields, as we can see in Fig. 3.3. This clearly does not meet our expectations, as for a strong magnetic field, the linear behavior of the transverse resistivity becomes a stepwise ascent, whereas the longitudinal resistivity features distinct peaks every time ρ_{xy} jumps up one step.

The difference in resistivity between two of these plateaus is exactly $R_K = \frac{h}{e^2}$ with R_K being the Klitzing constant. In fact, the quantization of the resistivity is exceedingly precise and easily measurable with modern means so that the Klitzing constant R_K serves as a norm for the resistance.

Notice, that in two dimensions resistance R and resistivity ρ , as well as conductance and conductivity are the same thing, as R and ρ are related by

$$R = \rho^{2-d} \quad (3.11)$$

with d being the dimension of space.

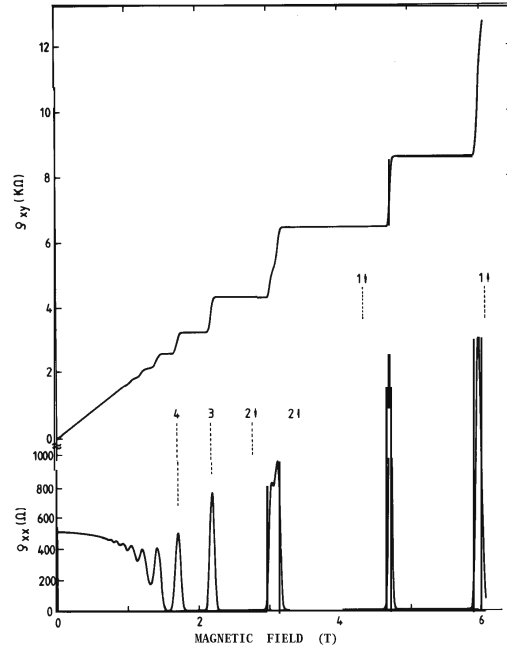


Fig. 3.3: Experimental resistivities ρ_{xx} and ρ_{xy} of a Hall system as a function of the magnetic field [10].

3.2.2 Landau levels

To understand this behavior, we consider the Hamiltonian of a charged particle coupled to an external magnetic field \mathbf{B} in z -direction and an electric field \mathbf{E} in the x -direction. As a gauge we choose the Landau gauge $\mathbf{A} = (0, Bx, 0)^\top$. We get

$$H = \frac{1}{2m}(p_x^2 + (p_y + eBx)^2) - eEx. \quad (3.12)$$

This is a well-known Hamiltonian leading to the strongly degenerate Landau levels. Having added the electric field, the degeneracies are lifted and the Hamiltonian above yields the following spectrum

$$E_{nk} = \hbar\omega_0 \left(n + \frac{1}{2} \right) + eE \left(k_y \lambda^2 - \frac{eE}{m\omega_0^2} \right) + \frac{m}{2} \frac{E^2}{B^2} \quad (3.13)$$

with λ being the magnetic length defined as

$$\lambda = \frac{\hbar}{eB}. \quad (3.14)$$

It is worth noting that the states drift neither in the \mathbf{E} - nor in the \mathbf{B} -direction, but in the $\mathbf{E} \times \mathbf{B}$ -direction with the group velocity being

$$v_y = \frac{1}{\hbar} \frac{\partial E_{nk}}{\partial k_y} = e\hbar E \lambda^2 = \frac{E}{B}. \quad (3.15)$$

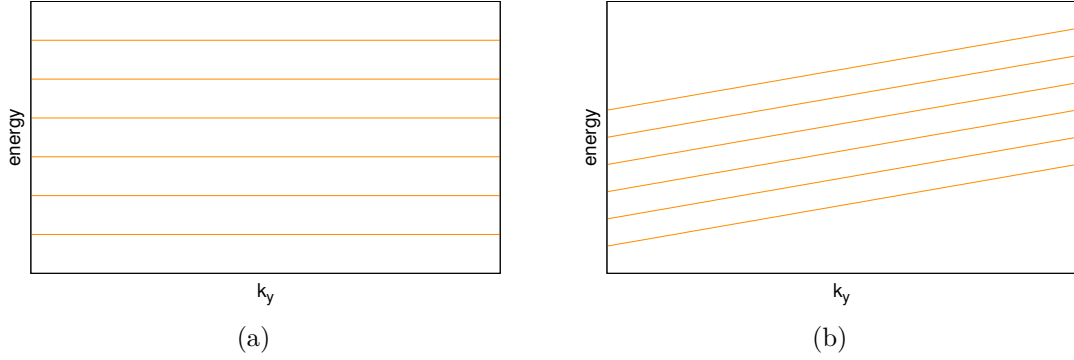


Fig. 3.4: (a) non-dispersive, degenerate Landau levels that result from the coupling to a magnetic field \mathbf{B} ; (b) electric field \mathbf{E} has been added, which lifts the degeneracies and makes the electrons disperse linearly.

We can think of the third term of (3.13) as the kinetic energy while the middle part corresponds to the potential energy of a wave packet, now localized around $-k_y\lambda^2 + eE/m\omega_0^2$.

Let us assume the Fermi energy sits between the first two Landau levels and vary the strength of the magnetic field \mathbf{B} adiabatically. Remember that the spacing between the Landau levels, or rather the cyclotron frequency ω_0 , is proportional to \mathbf{B} (3.4), so via changing \mathbf{B} we can shift the Fermi Energy up and down. Since the Landau energy levels are linearly dependent on k_y , each intersection of the Fermi energy with a Landau energy level contributes a fixed amount of conductivity to the overall Hall conductivity σ_{xy} , independently of where this intersection is. In Fig. 3.5 we can see two differently placed Fermi energies and their intersections with the Landau levels. Since the upper Fermi energy has overstepped one more level it has one more intersection and thereby the Hall conductivity is larger by $\frac{e^2}{2\pi\hbar}$.

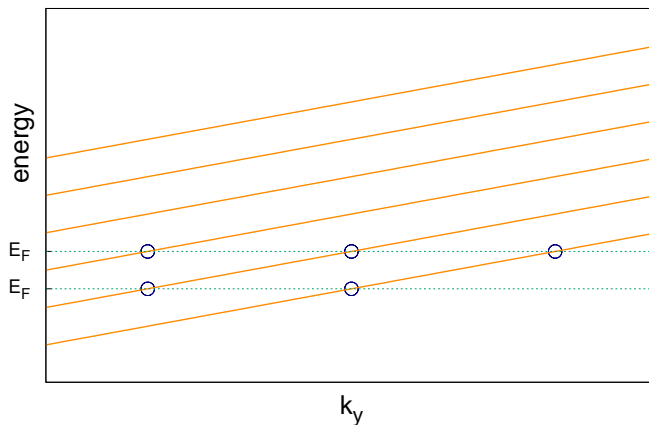


Fig. 3.5: Linearly dispersing Landau levels that are intersected by two different Fermi levels, resulting in a different number of nodes (blue circles).

3.3 Classical edge states

It can be shown experimentally that these conducting states are not evenly distributed over the sample, but they are localized exclusively at the boundary of the system.

Classical arguments, meaning not considering topology, can be given to explain this phenomenon.

Up to now, we have only considered periodic boundary conditions. Let us now factor in that the boundaries of our material are in fact open, so that we have a potential well with very steep walls (see Fig. 3.6) which makes the Landau bands bend upwards sharply at the edge of the system. As k_y and x are proportional to each other (3.13), with the

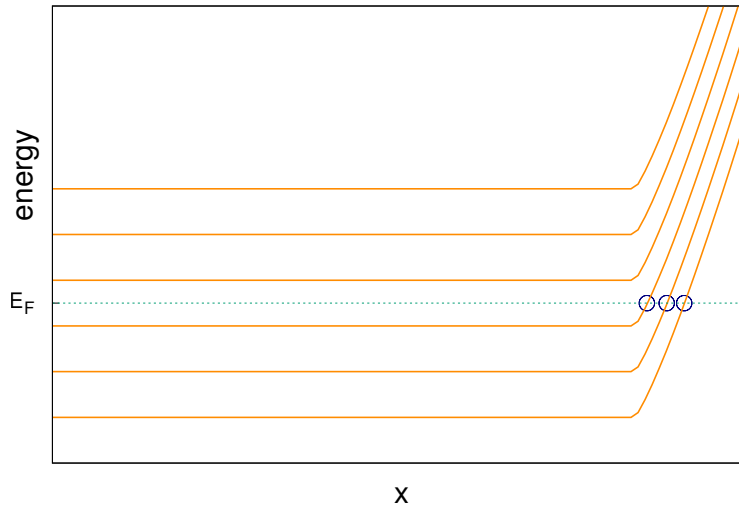


Fig. 3.6: Bent Landau levels in a potential well. The intersections of the bands with the arbitrarily set Fermi energy are located at the boundary.

proportionality constant being λ^2 , we are able to consider the energy spectrum in real space representation and see that indeed all of the intersections are located at boundaries of the sample.

Regarding the quantization of the Hall conductivity σ_{xy} , the same argument holds as in the previous section. However, looking at Fig. 3.6, we would argue that the bulk of our material is an insulator whereas the edges are metallic because that is where our intersections with the (arbitrarily chosen) Fermi energy sit.

Another way of understanding the appearance of conducting edge states in a classical fashion is to think about the cyclotron orbits of the particles. In the bulk of the material the particles will just describe a circular movement due to the applied magnetic field and the resulting Lorentz force. On the edges, however, the open boundaries of our system put a constraint on their movement. Imagine the particles bouncing off the boundary and thereby moving on *skipping orbits* (see Fig. 3.7). This results in an overall, chiral charge transport along the edges of our system.

This behavior can also account for the robustness of the effect. If the edges are the only places where charge is transported, the electrons have to travel a macroscopical distance (namely the width of the sample) in order to scatter other electrons.

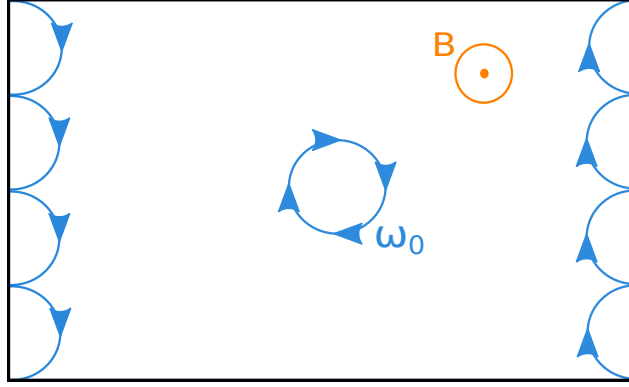


Fig. 3.7: Particles tracing circular trajectories due to the magnetic field \mathbf{B} and the resulting Lorentz force. Along the boundaries they are constrained to perform skipping orbits.

3.4 Kubo Formula

Putting aside the previous discussions for a while, we should now think of how to calculate the Hall conductivity. To this end, yet another technique has to be introduced.

The Kubo formula expresses the *linear response* of an observable quantity due to a time-dependent perturbation [14]. Let H_0 be our unperturbed Hamiltonian and $|m\rangle$ its energy eigenstates with

$$H_0 |m\rangle = E_m |m\rangle. \quad (3.16)$$

We now add a perturbation in the form of

$$\Delta H = -\mathbf{J}\mathbf{A} \quad (3.17)$$

with \mathbf{J} as the current density operator and \mathbf{A} as the electro-magnetic potential. We choose as gauge

$$\mathbf{A}_t = 0 \quad \Rightarrow \quad -\partial_t \mathbf{A} = \mathbf{E}. \quad (3.18)$$

Ultimately, we would like to consider a DC, but it is easier to work with an AC first and then take the limit $\omega \rightarrow 0$, where ω is the frequency of the current. We get

$$\mathbf{E}(t) = \mathbf{E}e^{-i\omega t} \quad \text{and} \quad \mathbf{A} = \frac{\mathbf{E}}{i\omega}e^{-i\omega t} \quad (3.19)$$

In the following we will work in the Dirac Picture, so that operators evolve with $\mathbf{J}(t) = V^{-1}\mathbf{J}V$ with $V = e^{-iH_0 t/\hbar}$, but the states with

$$|\psi(t)\rangle_D = U(t, t_0) |\psi(t_0)\rangle_D, \quad (3.20)$$

$$U(t, t_0) = e^{-\frac{i}{\hbar} \int_{t_0}^t \Delta H(t') dt'}. \quad (3.21)$$

Let us assume the system in its ground state $|\psi_0\rangle$ at time $t \rightarrow -\infty$.

$$\langle \mathbf{J}(t) \rangle = \langle \psi_0(t) | \mathbf{J}(t) | \psi_0(t) \rangle = \langle \psi_0 | U^{-1}(t) \mathbf{J}(t) U(t) | \psi_0 \rangle \quad (3.22)$$

$$\approx \langle \psi_0 | \frac{i}{\hbar} \int_{-\infty}^t dt' [\Delta H(t'), \mathbf{J}(t)] | \psi_0 \rangle \quad (3.23)$$

where we have used the time evolution of the states $\langle \psi_0 |$ and $|\psi_0\rangle$, as well as the linear expansion of $U(t)$ while assuming that the zeroth order vanishes. Combining (3.17) and (3.19) we get

$$\langle J_i(t) \rangle = \frac{1}{\hbar\omega} \int_{-\infty}^t dt' \langle \psi_0 | [J_j(t'), J_i(t)] | \psi_0 \rangle E_j e^{-i\omega t'} \quad (3.24)$$

and due to the system's time-translational invariance, we can write this expression as

$$\langle J_i(t) \rangle = \frac{1}{\hbar\omega} \left(\int_0^\infty dt'' e^{i\omega t''} \langle \psi_0 | [J_j(0), J_i(t'')] | \psi_0 \rangle \right) E_j e^{-i\omega t}. \quad (3.25)$$

As we can see, the current responds by oscillating at the same frequency ω when an electric field with that frequency is applied. The proportionality constant corresponds to our Hall conductivity. We are interested in the off-diagonal part, which is the *Kubo formula* for the Hall conductivity

$$\sigma_{xy}(\omega) = \frac{1}{\hbar\omega} \int_0^\infty dt e^{i\omega t} \langle \psi_0 | [J_y(0), J_x(t)] | \psi_0 \rangle. \quad (3.26)$$

Now we take into account that the current operator evolves as $\mathbf{J}(\mathbf{t}) = V^{-1} \mathbf{J} V$ with $V = e^{-iH_0 t/\hbar}$ and insert complete basis sets of the eigenstates of H_0 :

$$\begin{aligned} \sigma_{xy}(\omega) = \frac{1}{\hbar\omega} \int_0^\infty dt e^{i\omega t} \sum_n \langle \psi_0 | J_y | n \rangle \langle n | J_x | \psi_0 \rangle e^{i(E_n - E_0)t/\hbar} \\ - \sum_n \langle \psi_0 | J_x | n \rangle \langle n | J_y | \psi_0 \rangle e^{i(E_0 - E_n)t/\hbar} \end{aligned} \quad (3.27)$$

Before we perform the integral, we should substitute ω with $\omega + i\epsilon$ in order to circumvent poles on the real axis. After the integration we take the limit $\epsilon \rightarrow 0$. Doing this yields the following expression:

$$\sigma_{xy}(\omega) = -i \frac{1}{\omega} \sum_{n \neq 0} \left(\frac{\langle \psi_0 | J_y | n \rangle \langle n | J_x | \psi_0 \rangle}{\hbar\omega + E_n - E_0} - \frac{\langle \psi_0 | J_x | n \rangle \langle n | J_y | \psi_0 \rangle}{\hbar\omega + E_0 - E_n} \right) \quad (3.28)$$

In the DC Limit $\omega \rightarrow 0$ the denominators become

$$\frac{1}{\hbar\omega + E_n - E_0} \approx \frac{1}{E_n - E_0} - \frac{\hbar\omega}{(E_n - E_0)^2} + \mathcal{O}(\omega^2). \quad (3.29)$$

Assuming rotational invariance (or conservation of current) it can be shown, that the

zeroth order terms must vanish. We are left with

$$\sigma_{xy} = i\hbar \sum_{n \neq 0} \frac{\langle \psi_0 | J_y | n \rangle \langle n | J_x | \psi_0 \rangle - \langle \psi_0 | J_x | n \rangle \langle n | J_y | \psi_0 \rangle}{(E_n - E_0)^2}. \quad (3.30)$$

3.5 Hall conductivity as a Chern number

Finally, we are in a position to combine what we have learned so far and show the relationship between the Hall conductivity σ_{xy} and topology.

Let us consider a cubic lattice with lattice constant a and periodic boundary conditions. We will neglect electron-electron interaction, so the wavefunctions in a given band n can be given by Bloch waves

$$\psi_{\mathbf{k}}^n(\mathbf{x}) = e^{i\mathbf{k}\mathbf{x}} u_{\mathbf{k}}^n(\mathbf{x}) \quad (3.31)$$

with $u_{\mathbf{k}}^n(\mathbf{x})$ being periodic on the unit cell. Furthermore, we will assume that we are dealing with an insulator at $T = 0$, so that all bands below E_F are completely filled and those above are completely empty. Let us examine the matrix elements of the Berry connection (2.9)

$$\mathcal{A}_i^n = i \langle u_{\mathbf{k}}^n | \frac{\partial}{\partial k_i} | u_{\mathbf{k}}^n \rangle. \quad (3.32)$$

We can see that a $U(1)$ gauge transformation of \mathcal{A} corresponds to a change of phase of $|u_{\mathbf{k}}^n\rangle$. Calculating the corresponding Berry curvature, we arrive at

$$\mathcal{F}_{xy} = \frac{\partial \mathcal{A}_y}{\partial k_x} - \frac{\partial \mathcal{A}_x}{\partial k_y} = i \langle \frac{\partial u_{\mathbf{k}}^n}{\partial k_x} | \frac{\partial u_{\mathbf{k}}^n}{\partial k_y} \rangle - i \langle \frac{\partial u_{\mathbf{k}}^n}{\partial k_y} | \frac{\partial u_{\mathbf{k}}^n}{\partial k_x} \rangle. \quad (3.33)$$

The Chern number for our two-dimensional system is given by

$$C = \frac{1}{2\pi} \int_{BZ} d^2k \mathcal{F}_{xy}. \quad (3.34)$$

For particles on the lattice the Kubo formula (3.30) becomes

$$\sigma_{xy} = i\hbar \sum_n \sum_m \int_{BZ} \frac{d^2k d^2k'}{(2\pi)^4} \frac{\langle u_{\mathbf{k}}^n | J_y | u_{\mathbf{k}'}^m \rangle \langle u_{\mathbf{k}'}^m | J_x | u_{\mathbf{k}}^n \rangle - \langle u_{\mathbf{k}}^n | J_x | u_{\mathbf{k}'}^m \rangle \langle u_{\mathbf{k}'}^m | J_y | u_{\mathbf{k}}^n \rangle}{(E_m(\mathbf{k}) - E_n(\mathbf{k}))^2} \quad (3.35)$$

where n runs over the filled bands and m runs over *all* bands, such that the following completeness relation is fulfilled:

$$\sum_m \int_{BZ} \frac{d^2k'}{(2\pi)^2} |u_{\mathbf{k}'}^m\rangle \langle u_{\mathbf{k}'}^m| = \mathbf{1} \quad (3.36)$$

Let us define \mathbf{J} in terms of the group velocity of the wave packet:

$$\mathbf{J} = \frac{e}{\hbar} \frac{\partial H}{\partial \mathbf{k}} \quad (3.37)$$

We would like to work with $|u_{\mathbf{k}}^n\rangle$ rather than with $|\psi_{\mathbf{k}}^n\rangle$, so we take a look at the eigenproblem of our Bloch functions again and define

$$\begin{aligned} H_0 |\psi_{\mathbf{k}}^n\rangle &= E_n(\mathbf{k}) |\psi_{\mathbf{k}}^n\rangle \Rightarrow e^{-i\mathbf{k}\mathbf{x}} H_0 e^{i\mathbf{k}\mathbf{x}} |u_{\mathbf{k}}^n\rangle \\ &\Rightarrow H |u_{\mathbf{k}}^n\rangle = E_n(\mathbf{k}) |u_{\mathbf{k}}^n\rangle \end{aligned}$$

where we set $H = e^{-i\mathbf{k}\mathbf{x}} H_0 e^{i\mathbf{k}\mathbf{x}}$. The Kubo formula becomes

$$\sigma_{xy} = \frac{ie^2}{\hbar} \sum_n \sum_m \int_{BZ} \frac{d^2k \, d^2k'}{(2\pi)^4} \frac{\langle u_{\mathbf{k}}^n | \partial_y H | u_{\mathbf{k}'}^m \rangle \langle u_{\mathbf{k}'}^m | \partial_x H | u_{\mathbf{k}}^n \rangle - \langle u_{\mathbf{k}}^n | \partial_x H | u_{\mathbf{k}'}^m \rangle \langle u_{\mathbf{k}'}^m | \partial_y H | u_{\mathbf{k}}^n \rangle}{(E_m(\mathbf{k}) - E_n(\mathbf{k}))^2} \quad (3.38)$$

with $\partial_x \equiv \frac{\partial}{\partial k_x}$ and $\partial_y \equiv \frac{\partial}{\partial k_y}$. For i being either x or y respectively, consider the product rule

$$\begin{aligned} \langle u_{\mathbf{k}}^n | \partial_i (H | u_{\mathbf{k}'}^m \rangle) &= \langle u_{\mathbf{k}}^n | \partial_i H | u_{\mathbf{k}'}^m \rangle + \langle u_{\mathbf{k}}^n | H | \partial_i u_{\mathbf{k}'}^m \rangle \\ \Leftrightarrow \langle u_{\mathbf{k}}^n | \partial_i H | u_{\mathbf{k}'}^m \rangle &= \langle u_{\mathbf{k}}^n | \partial_i (H | u_{\mathbf{k}'}^m \rangle) - \langle u_{\mathbf{k}}^n | H | \partial_i u_{\mathbf{k}'}^m \rangle \\ &= (E_m(\mathbf{k}') - E_n(\mathbf{k})) \langle u_{\mathbf{k}}^n | \partial_i u_{\mathbf{k}'}^m \rangle \\ &= -(E_m(\mathbf{k}') - E_n(\mathbf{k})) \langle \partial_i u_{\mathbf{k}}^n | u_{\mathbf{k}'}^m \rangle \end{aligned}$$

Substituting this into the Kubo formula (3.30) yields

$$\sigma_{xy} = \frac{ie^2}{\hbar} \sum_n \int_{BZ} \frac{d^2k}{(2\pi)^2} \langle \partial_x u_{\mathbf{k}}^n | \partial_y u_{\mathbf{k}}^n \rangle - \langle \partial_y u_{\mathbf{k}}^n | \partial_x u_{\mathbf{k}}^n \rangle. \quad (3.39)$$

With (3.33) and (3.34) we finally get

$$\sigma_{xy} = \frac{e^2}{\hbar} \sum_n \int_{BZ} \frac{d^2k}{(2\pi)^2} \mathcal{F}_{xy} \quad (3.40)$$

$$= \frac{e^2}{2\pi\hbar} \sum_n C_n. \quad (3.41)$$

This equation states that the Hall conductivity σ_{xy} is the sum over the Chern numbers of the filled bands of our material (with the exception of some prefactor). We see that the behavior of such a system is a manifestly topological property, which can account for the robustness of the effect.

3.6 Topological edge states

In the last section, we saw that the Hall conductivity is a topological invariant and it has also been discussed that the states which contribute to the overall Hall conductivity σ_{xy} live on the edges of our system. We have also learned that we can explain this behavior by considering the bending of the Landau levels due to the two-dimensional-box potential of the system. The previous calculation enables us to discuss the appearance of the edge conductivity under a new aspect.

In the same way as no homeomorphism between two objects with different genera can be found, the band structures of materials belonging to different Chern classes can not be adiabatically transformed into one another. At the transition between two insulating materials, having two different Chern numbers, metallic edge states appear in order to have a smooth transition between a topological non-trivial and a trivial material (e.g. vacuum).

Imagine two bands that have to unwind in order to unravel a knot representing the topological non-triviality (see Fig. 3.8). This is not possible without closing the band gap somewhere, which is why the topological non-trivial material becomes metallic at the edges.

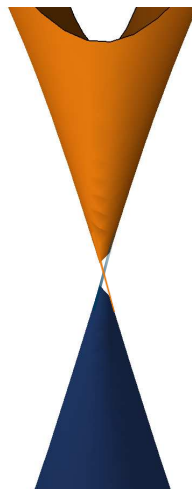


Fig. 3.8: A "twist" between two bands renders the material topological non-trivial.

4 Density functional theory

Density functional theory (DFT) is the most widely used tool for the calculation of electronic structure in solids. The foundation of this method is that every observable or property of an interacting, many-particle system can be derived from the ground state density $n_0(\mathbf{r})$. Any quantity can be treated as a functional of $n_0(\mathbf{r})$, which contains, in theory, all the information about the many-body wave function.

However, no exact functionals for any many-particle or even two-particle systems are known. It was the famous ansatz of Kohn and Sham which finally enabled physicists to make useful approximations for ground state functionals. Their ansatz maps the real, interacting many-body system to an auxiliary system of non-interacting particles. The many-particle effects are contained in the so-called *exchange-correlation* functional.

4.1 Hohenberg-Kohn Theorems

For a system of N interacting particles, the Hamiltonian can be written as

$$H = -\frac{\hbar^2}{2m_e} \sum_{i=1}^N \nabla_i^2 + \sum_{i=1}^N V_{ext}(\mathbf{r}_i) + \frac{1}{2} \sum_{\substack{i,j=0 \\ i \neq j}}^N \frac{e^2}{|\mathbf{r}_i - \mathbf{r}_j|}. \quad (4.1)$$

As we know, no exact solution for this Hamiltonian can be obtained if N exceeds only a few particles, neither analytically, nor numerically. This is far below the 10^{23} particles a solid usually consists of. Thus, only with drastic simplifications we are able to gain access to certain approximate solutions. This is where density functional theory comes into play. The foundation on which DFT is based upon are two theorems first proposed by Hohenberg and Kohn [15] and applies to any system of N interacting particles in an external potential $V_{ext}(\mathbf{r})$:

- **Theorem 1:** For any interacting many-body system in an external potential $V_{ext}(\mathbf{r})$, the ground state density $n_0(\mathbf{r})$ uniquely determines $V_{ext}(\mathbf{r})$, up to a constant.
- **Theorem 2:** For any $V_{ext}(\mathbf{r})$ an energy functional $E[n(\mathbf{r})]$ exists and choosing a fixed $V_{ext}(\mathbf{r})$, the minimum of $E[n(\mathbf{r})]$ is the exact ground state energy of the system, which is found at $n(\mathbf{r}) = n_0(\mathbf{r})$.

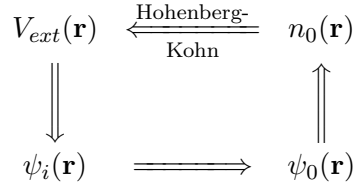


Fig. 4.1: Assuming we know the external potential $V_{ext}(\mathbf{r})$, our Hamiltonian H is fully determined, which means we are able to determine its set of wave functions $\psi_i(\mathbf{r})$, in principle. The wave function $\psi_0(\mathbf{r})$, belonging to the ground state energy value, is contained in this set. With $\psi_0(\mathbf{r})$ at hand, any observable can be calculated, including the ground state density $n_0(\mathbf{r})$. The Hohenberg-Kohn theorem states, though, that $n_0(\mathbf{r})$ completely determines the external potential $V_{ext}(\mathbf{r})$, and thus closes the circle.

4.1.1 Proof of theorem 1

Let us now consider the first theorem and proof it by contradiction:

Suppose there are two different external potentials $V_{ext}(\mathbf{r})$ and $V'_{ext}(\mathbf{r})$ which both yield the same ground state density $n_0(\mathbf{r})$. Of course, different potentials lead to different Hamiltonians H and H' with their ground state wave functions $\psi_0(\mathbf{r})$ and $\psi'_0(\mathbf{r})$. Knowing that the energy obtained by the exact ground state wave function sets a lower bound for the energy spectrum and taking into account that $\psi'_0(\mathbf{r})$ is no eigenfunction of H it follows that

$$E = \langle \psi_0(\mathbf{r}) | H | \psi_0(\mathbf{r}) \rangle < \langle \psi'_0(\mathbf{r}) | H | \psi'_0(\mathbf{r}) \rangle \quad (4.2)$$

where we assumed that the ground state is non-degenerate. This assumption is not necessary and the proof can be extended to cover degenerate cases as well [16]. The right side of the inequality can be expressed as

$$\begin{aligned}
 \langle \psi'_0(\mathbf{r}) | H | \psi'_0(\mathbf{r}) \rangle &= \langle \psi'_0(\mathbf{r}) | H' | \psi'_0(\mathbf{r}) \rangle - \langle \psi'_0(\mathbf{r}) | H - H' | \psi'_0(\mathbf{r}) \rangle \\
 &= E' + \int_V d^3r \left[V_{ext}(\mathbf{r}) - V'_{ext}(\mathbf{r}) \right] n_0(\mathbf{r}) \\
 \Rightarrow \quad E &< E' + \int_V d^3r \left[V_{ext}(\mathbf{r}) - V'_{ext}(\mathbf{r}) \right] n_0(\mathbf{r})
 \end{aligned} \quad (4.3)$$

If we choose the following equation as our starting point

$$E' = \langle \psi'_0(\mathbf{r}) | H' | \psi'_0(\mathbf{r}) \rangle < \langle \psi_0(\mathbf{r}) | H' | \psi_0(\mathbf{r}) \rangle \quad (4.4)$$

we will arrive at

$$E' < E + \int_V d^3r \left[V'_{ext}(\mathbf{r}) - V_{ext}(\mathbf{r}) \right] n_0(\mathbf{r}). \quad (4.5)$$

Adding 4.3 and 4.5 we arrive at the contradiction

$$E + E' < E + E'. \quad (4.6)$$

This means the ground state density $n_0(\mathbf{r})$ determines the external potential $V_{ext}(\mathbf{r})$ uniquely up to a constant shift.

4.1.2 Proof of theorem 2

Let us restrict ourselves to the subspace of densities $n(\mathbf{r})$ that only contains the so-called *V-representable* densities. Those are densities that are ground state densities of H with any external potential V_{ext} . Since all quantities of the system are uniquely determined by $n(\mathbf{r})$, the functional becomes linearly separable such that

$$E[n(\mathbf{r})] = E_0[n(\mathbf{r})] + \int_V d^3r V_{ext}(\mathbf{r})n(\mathbf{r}) + E_{nuc} \quad (4.7)$$

where E_0 contains all the internal energies, i.e. the kinetic and the potential terms and E_{nuc} is the interaction energy of the nuclei.

Because E_0 is a functional of the particle density $n(\mathbf{r})$ only, it must be *universal* by construction, meaning independent of the external potential $V_{ext}(\mathbf{r})$ and thus the same for all electron systems.

Now suppose there is a ground state density $n_0(\mathbf{r})$ corresponding to the external potential $V_{ext}(\mathbf{r})$ and the ground state wave function $\psi_0(\mathbf{r})$, so

$$E = E[n_0(\mathbf{r})] = \langle \psi_0(\mathbf{r}) | H | \psi_0(\mathbf{r}) \rangle. \quad (4.8)$$

For a different ground state density $n'_0(\mathbf{r})$ and its ground state wave function $\psi'_0(\mathbf{r})$, we necessarily get a greater energy.

$$E = \langle \psi_0(\mathbf{r}) | H | \psi_0(\mathbf{r}) \rangle < \langle \psi'_0(\mathbf{r}) | H | \psi'_0(\mathbf{r}) \rangle = E'. \quad (4.9)$$

Thus, if we knew the functional E , we could find the exact ground state energy and density by minimization.

4.2 Kohn-Sham ansatz

Since systems of interacting particles are difficult, if not impossible, to solve, Kohn and Sham provided an ansatz which replaces that problem with something that is more manageable [17]. They assume that there is some non-interacting system that has the same ground state density as the original one. Even large non-interacting systems are in practice solvable (numerically). The terms arising due to the many-body nature of the problem are put into the exchange-correlation functional that was mentioned in the introduction of this chapter.

The accuracy of the obtained ground state energy and density is only limited by the approximations concerning the exchange-correlation functional.

We choose the Hamiltonian of the auxiliary system such that it consists of the kinetic term T and an effective local potential V_{KS}^σ , acting on an electron of spin σ at \mathbf{r} . Using the Hartree units, the Hamiltonian takes the form

$$H_{KS}^\sigma = -\frac{1}{2}\nabla^2 + V_{KS}^\sigma(\mathbf{r}). \quad (4.10)$$

Let us now collect all the necessary terms to build the functional. The density is given by the square of all the orbitals $\psi_i^\sigma(\mathbf{r})$

$$n(\mathbf{r}) = \sum_{\sigma} \sum_{i=1}^N |\psi_i^\sigma(\mathbf{r})|^2 \quad (4.11)$$

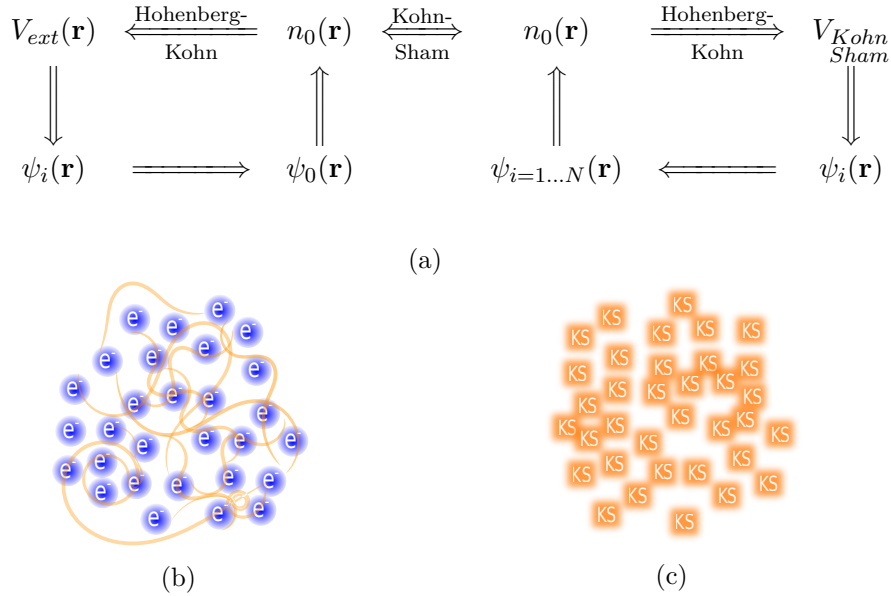


Fig. 4.2: (a) on the left hand side we recognize Fig. 4.1, which is linked to the auxiliary system by the Kohn-Sham ansatz. As the right system is non-interacting, we get a separate one-particle wave function for each particle; (b) depiction of an interacting system of electrons; (c) a non-interacting system of particles that has the same ground state density as system (b) does.

and T can be calculated by

$$T = \frac{1}{2} \sum_{\sigma} \sum_{i=1}^N |\nabla \psi_i^{\sigma}(\mathbf{r})|^2. \quad (4.12)$$

Naturally, we have to consider the interaction of the charged particles via the Coulomb repulsion. This energy functional is called the Hartree energy and is just the classical Coulomb interaction of the electron density

$$E_H[n(\mathbf{r})] = \frac{1}{2} \int_V d^3r \int_V d^3r' \frac{n(\mathbf{r})n(\mathbf{r}')}{|\mathbf{r} - \mathbf{r}'|}. \quad (4.13)$$

Now, we have everything we need in order to rewrite the Hohenberg-Kohn functional (4.7) as

$$E_{KS}[n(\mathbf{r})] = T[n(\mathbf{r})] + \int_V d^3r V_{ext}(\mathbf{r})n(\mathbf{r}) + E_H[n(\mathbf{r})] + E_{int.} + E_{xc}[n(\mathbf{r})]. \quad (4.14)$$

$V_{ext}(\mathbf{r})$ contains the potential of the nuclei and is well-defined, just as E_H and E_{nuc} . As previously mentioned, all many-body effects are contained in E_{xc} . Comparing E_{KS} to the Hohenberg-Kohn functional (4.7), we see that the exchange-correlation functional can be written as

$$\begin{aligned} E_{xc}[n(\mathbf{r})] &= E_0[n(\mathbf{r})] - T[n(\mathbf{r})] - E_H[n(\mathbf{r})] \\ &= \langle T_0 \rangle - T[n(\mathbf{r})] + \langle V_{int} \rangle - E_H[n(\mathbf{r})]. \end{aligned} \quad (4.15)$$

The latter equation shows that E_{xc} is just the difference between the energies of the real and the auxiliary system. Still, we do not know the exact form of the exchange-correlation functional, but finding a reasonable approximation for E_{xc} will finally enable us to calculate the ground state properties of the interacting many-body system.

We have demonstrated that the minimum of our energy functional yields the exact ground state energy and density (see Sec. 4.1.2). Minimizing E_{KS} , under the constraint of $\psi_i^\sigma(\mathbf{r})$ being normalized, gives the *Kohn-Sham-equations*:

$$(H_{KS}^\sigma(\mathbf{r}) - \varepsilon_i^\sigma) \psi_i^\sigma(\mathbf{r}) = 0 \quad (4.16)$$

H_{KS}^σ has already been introduced in (4.10). ε_i^σ are the energy eigenvalues and $V_{KS}^\sigma(\mathbf{r})$, which we have not specified earlier, has now been identified as

$$\begin{aligned} V_{KS}^\sigma(\mathbf{r}) &= V_{ext}(\mathbf{r}) + \frac{\delta E_H[n(\mathbf{r})]}{\delta n'(\mathbf{r})} + \frac{\delta E_{xc}[n(\mathbf{r})]}{\delta n'(\mathbf{r})} \\ &= V_{ext}(\mathbf{r}) + V_H(\mathbf{r}) + V_{xc}^\sigma(\mathbf{r}). \end{aligned} \quad (4.17)$$

Notice that the spin-dependency of $n(\mathbf{r})$ has been omitted so far, but appears now explicitly as an index of $V_{xc}^\sigma(\mathbf{r})$. As we still do not know the form of E_{xc} , we are forced to consider approximate forms of this functional to get any further. It is reasonable to approximate E_{xc} as a local or nearly local functional of the density:

$$E_{xc}[n(\mathbf{r})] = \int_V d^3r n(\mathbf{r}) \varepsilon_{xc}([n], \mathbf{r}) \quad (4.18)$$

This means that the energy per electron ε_{xc} only depends on the density $n(\mathbf{r})$ in a small area around the point \mathbf{r} . ε_{xc} can be related to the so-called exchange-correlation. To see this, we will vary our Hamiltonian adiabatically in parameter space and calculate the change in energy, which reads

$$\Delta E = \int_{\lambda_1}^{\lambda_2} d\lambda \frac{dE}{d\lambda} = \int_{\lambda_1}^{\lambda_2} d\lambda \langle \psi_\lambda | \frac{dH}{d\lambda} | \psi_\lambda \rangle. \quad (4.19)$$

We will vary λ from 0 to 1, which is equivalent to connecting the non-interacting system smoothly with the interacting one, as in Hartree units $e = 1$ and therefore $e^2 = 1$. Basically, we are turning on the interaction slowly by progressively increasing the coupling constant e^2 of the interaction. For a constant density $n(\mathbf{r})$, all the terms in (4.15), except for V_{int} , will remain constant too. Hence this integral yields

$$E_{xc}[n(\mathbf{r})] = \int_0^{e^2} d\lambda \langle \psi_\lambda | \frac{d}{d\lambda} | \psi_\lambda \rangle - E_H[n(\mathbf{r})] = \frac{1}{2} \int_V d^3r n(\mathbf{r}) \int_V d^3r' \frac{\bar{n}_{xc}(\mathbf{r}, \mathbf{r}')}{|\mathbf{r} - \mathbf{r}'|} \quad (4.20)$$

with

$$\bar{n}_{xc}(\mathbf{r}, \mathbf{r}') = \int_0^1 d\lambda n_{xc}^\lambda(\mathbf{r}, \mathbf{r}'). \quad (4.21)$$

$n_{xc}^\lambda(\mathbf{r}, \mathbf{r}')$ is the exchange-correlation hole, which we averaged above with respect to the coupling constant e^2 . Together, (4.18) and (4.20) allow us to write the exchange-correlation density ε_{xc} as

$$\varepsilon_{xc}([n], \mathbf{r}) = \frac{1}{2} \int_V d^3r' \frac{\bar{n}_{xc}(\mathbf{r}, \mathbf{r}')}{|\mathbf{r} - \mathbf{r}'|}. \quad (4.22)$$

Fundamentally, ε_{xc} is the average change of the potential energy due to the exchange-correlation hole when varying from no correlation at all to the real, fully-correlated system.

Considering (4.17) and applying the product rule, we can write the exchange-correlation potential $V_{xc}^\sigma(\mathbf{r})$ as

$$V_{xc}^\sigma(\mathbf{r}) = \varepsilon_{xc}([n], \mathbf{r}) + n(\mathbf{r}) \frac{\delta \varepsilon_{xc}([n], \mathbf{r})}{\delta n'(\mathbf{r})}. \quad (4.23)$$

The second term in the equation above is called response potential because it describes the change of the exchange-correlation hole $n_{xc}^\lambda(\mathbf{r}, \mathbf{r}')$ with the density $n(\mathbf{r})$. As this term is discontinuous at the band gap, adding a single electron to the system changes the potential by a constant amount. This can easily be understood considering the kinetic energy T , which must change unsteadily too when a transition from an occupied to an empty band occurs. Therefore, the functional $T[n]$ has discontinuous derivatives at densities that correspond to filled bands, which is very hard to incorporate into a density functional. Hence, these effects will not occur for the simpler approximate functional that is introduced in the next section and is used for our calculations later on.

4.3 Perdew-Burke-Ernzerhof generalized-gradient approximation

A special approach to construct the exchange-correlation functional E_{xc} has been introduced by Perdew, Burke and Ernzerhof (PBE) [18].

Typically, a generalized-gradient approximation (GGA) is a choice for E_{xc} which includes the gradient of the density ∇n^σ , whereas earlier approximations of E_{xc} , like local spin density approximation (LSDA), are merely functions of the density n .

- Local spin density approximation: $E_{xc} = E_{xc}^{LSDA}[n_\uparrow, n_\downarrow]$
- generalized gradient approximation $E_{xc} = E_{xc}^{GGA}[n_\uparrow, n_\downarrow, \nabla n_\uparrow, \nabla n_\downarrow]$

The hypernym generalized-gradient approximation denotes a range of functions that modify the behavior of large gradients in such a way that fits real materials best. Let us define the functional E_{xc}^{GGA} in a general form that is used for GGA:

$$E_{xc}^{GGA} = \int d^3r n(\mathbf{r}) \varepsilon_{xc}^{unif}(n) F_{xc} \quad (4.24)$$

where ε_{xc}^{unif} is the exchange-correlation energy of a uniform electron gas and F_{xc} is a dimensionless function that scales ε_{xc}^{unif} . While ε_{xc}^{unif} is well established [19], F_{xc} has to be chosen in a fashion that preserves the desired qualities best.

Perdew, Burke and Ernzerhof constructed the correlation part of the functional E_c^{GGA} from three conditions.

1. In the slowly varying limit $|\nabla n| \rightarrow 0$, the gradient contribution H of this functional is given by its second-order gradient expansion

$$H \rightarrow \alpha |\nabla n|^2. \quad (4.25)$$

2. In the rapidly varying limit $|\nabla n| \rightarrow \infty$,

$$H \rightarrow -\varepsilon_c^{unif} \quad (4.26)$$

making correlation necessarily vanish, as for very large gradients the sum rule is only satisfied by $n_c = 0$.

3. Under uniform scaling to the high density limit, the correlation energy must converge to a constant.

To model the exchange part of energy functional E_x^{GGA} , they took into account four more constraints to which E_x^{GGA} must oblige.

4. For the same limit as in condition 3 and a vanishing spin polarization everywhere, E_x^{GGA} must be of the same form as (4.24), with F_x only depending on a dimensionless density gradient $s = \frac{|\nabla n|}{2k_F n}$. Then, to recover the correct uniform gas limit, $F_x(0) = 1$ must obviously hold.
5. The exact exchange energy obeys the spin-scaling relationship

$$E_x[n_\uparrow, n_\downarrow] = \frac{1}{2} (E_x[2n_\uparrow] + E_x[2n_\downarrow]). \quad (4.27)$$

6. For the linear response of the spin-unpolarized uniform electron gas, i.e. for small variations of density around the uniform density, the linear response of the LSDA should be attained.
7. The so-called *Lieb-Oxford* bound should be satisfied [20]. It reads

$$E_X[n_\uparrow, n_\downarrow] \geq E_{XC}[n_\uparrow, n_\downarrow]. \quad (4.28)$$

Perdew, Burke and Ernzerhof managed to find a function F_{xc} that fulfills all of the requirements mentioned above and is given in their original paper [18].

Up to the present day, their model is implemented in a lot of codes and all the DFT calculations that will appear later on in this thesis have been calculated using PBE.

4.4 WIEN2k

WIEN2k is a DFT program package that allows to perform electronic structure calculations of solids. All the results on the electronic properties of graphene nanoribbons (GNR) that are presented later, are obtained using this code.

WIEN2k uses the linearized augmented plane wave (LAPW) method which is among the most accurate methods for performing DFT on crystals. Although this method is originally based on LSDA, it is also implemented for GGA.

With LAPW, the Kohn-Sham equations of a many-electron system can be calculated by introducing a basis set as an ansatz which has been adapted to the problem. To achieve this, the space is divided into non-overlapping regions centered around the atoms of the lattice and an interstitial region (see Fig.4.3). For each region a different basis set is used. In the interstitial region ordinary plane waves form our basis:

$$\phi_{\mathbf{k}_n} = \frac{1}{\sqrt{\omega}} e^{i\mathbf{k}_n \mathbf{r}} \quad (4.29)$$

\mathbf{k} is the crystal momentum inside the first Brillouin zone and $\mathbf{k}_n = \mathbf{k} + \mathbf{K}_n$ with \mathbf{K}_n as the set of reciprocal lattice vectors.

Inside the atomic spheres of a certain radius R , we choose linear combinations of radial functions multiplied with spherical harmonics $Y_{lm}(\mathbf{r})$.

$$\phi_{\mathbf{k}_n} = \sum_{lm} [A_{lm} u_l(r, E_l) + B_{lm} \dot{u}_l(r, E_l)] Y_{lm}(\mathbf{r}) \quad (4.30)$$

with $u_l(r, E_l)$ being the regular solution of the radial Schrödinger equation for energy E_l . The coefficients A_{lm} and B_{lm} are functions of \mathbf{k}_n and are determined by requiring that this basis function and its derivative connect smoothly to the basis functions of the interstitial region. The boundary conditions can also be chosen such that the coefficients A_{lm} and B_{lm} do not depend on \mathbf{k}_n , are normalized and equal zero at the sphere boundaries. This is called APW+lo, where "lo" stands for local orbitals [21]. Since these basis functions vanish abruptly at the boundaries, they have to be made smooth and differentiable again by adding surface terms.

u_l and its time derivative \dot{u}_l can be computed numerically on a radial mesh inside the sphere.

With these tools at hand, we can calculate all the relevant quantities for the systems that are to be examined later. Unfortunately, the GNR presented in [6] contain many atoms per unit cell. Although parallelization is used to distribute the work load over the university's cluster, the size of these structures exceeds our means, as the computational effort scales exponentially with the number of atoms. One of the main goals of this thesis is to reproduce the effects presented in [6] with GNR that are as small as possible and therefore easier to handle with DFT.

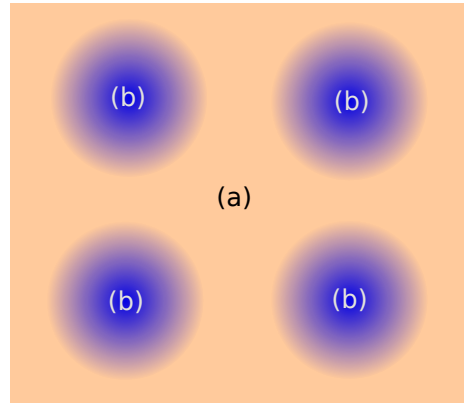


Fig. 4.3: (a): interstitial region
(b): atomic spheres

5 Graphene

In 2010 Andre Geim and Konstantin Novoselov were awarded with the Nobel Prize for the synthesis of the world's first 2D material: graphene [50]. Since then, graphene has been a very popular subject of research due to its interesting properties and the rich physics it provides.

Graphene is a semimetal and has a hexagonal lattice, which can be seen as two interleaving triangular lattices with A and B sites (see Fig.5.1a).

In this chapter we examine graphene's band structure and show that graphene features gapless Dirac fermions close to the Fermi level. Afterwards we investigate on its symmetries, which protect the system from opening a gap and becoming an insulator.

5.1 Electronic structure of graphene

5.1.1 Tight-binding

As we can see in Fig. 5.1a, graphene's hexagonal lattice has the following translation vectors

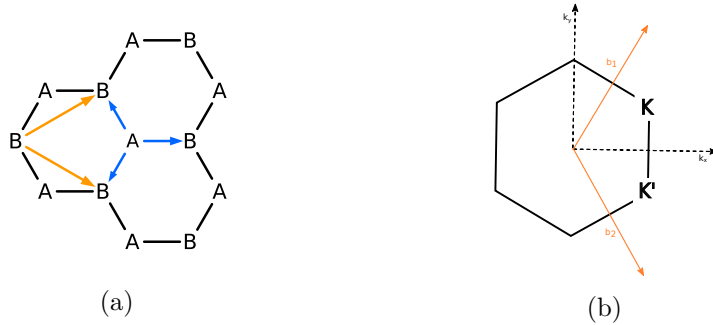


Fig. 5.1: (a) graphene lattice, its primitive vectors \mathbf{a}_1 , \mathbf{a}_2 (orange) and the hopping bonds $\boldsymbol{\delta}_1$, $\boldsymbol{\delta}_2$, $\boldsymbol{\delta}_3$ (blue); (b) first Brillouin zone, the \mathbf{K} -points and the reciprocal lattice vectors \mathbf{b}_1 and \mathbf{b}_2 .

$$\mathbf{a}_1 = \frac{a_0}{2} \begin{pmatrix} 3 \\ \sqrt{3} \end{pmatrix}, \quad \mathbf{a}_2 = \frac{a_0}{2} \begin{pmatrix} 3 \\ -\sqrt{3} \end{pmatrix} \quad (5.1)$$

with a_0 being the bond length. For real graphene $a_0 = 1.4245\text{\AA}$. Because the reciprocal lattice vectors \mathbf{b}_i need to satisfy $\mathbf{a}_i \mathbf{b}_j = 2\pi\delta_{ij}$, we get

$$\mathbf{b}_1 = \frac{2\pi}{3a_0} \begin{pmatrix} 1 \\ \sqrt{3} \end{pmatrix}, \quad \mathbf{b}_2 = \frac{2\pi}{3a_0} \begin{pmatrix} 1 \\ -\sqrt{3} \end{pmatrix}. \quad (5.2)$$

The vectors linking one site with its nearest neighbors are described by

$$\boldsymbol{\delta}_1 = \frac{a_0}{2} \begin{pmatrix} 1 \\ \sqrt{3} \end{pmatrix}, \quad \boldsymbol{\delta}_2 = \frac{a_0}{2} \begin{pmatrix} 1 \\ -\sqrt{3} \end{pmatrix}, \quad \boldsymbol{\delta}_3 = a_0 \begin{pmatrix} -1 \\ 0 \end{pmatrix}. \quad (5.3)$$

Taking into account only nearest-neighbor interactions, we can easily build the Hamiltonian, in which we initially neglect the system's spin degrees of freedom, as graphene's ground state is non-magnetic.

$$H = - \sum_{\mathbf{R}} \sum_{i=1}^3 \left[t_i b^\dagger(\mathbf{R} + \boldsymbol{\delta}_i) a(\mathbf{R}) + t_i a^\dagger(\mathbf{R}) b(\mathbf{R} + \boldsymbol{\delta}_i) \right] \quad (5.4)$$

where t_i is the hopping along the $\boldsymbol{\delta}_i$ and $a(\mathbf{R})$ and $b(\mathbf{R})$ are the annihilation operators on the A and B site respectively. The sum over \mathbf{R} implies summation over all sites $\mathbf{R} = n\mathbf{a}_1 + m\mathbf{a}_2$ with $n, m \in \mathbb{N}$. The Fourier transform of one of these operators is given by

$$a(\mathbf{R}) = \frac{1}{\sqrt{N}} \sum_{\mathbf{k}} e^{i\mathbf{k}\mathbf{R}} a_{\mathbf{k}}. \quad (5.5)$$

This leads to

$$H = - \frac{1}{N} \sum_{\mathbf{k}, \mathbf{q}} \sum_{\mathbf{R}} \sum_{i=1}^3 e^{i(\mathbf{k}-\mathbf{q})\mathbf{R}} \left[t_i e^{-i\mathbf{q}\boldsymbol{\delta}_i} b_{\mathbf{q}}^\dagger a_{\mathbf{k}} + t_i e^{i\mathbf{k}\boldsymbol{\delta}_i} a_{\mathbf{q}}^\dagger b_{\mathbf{k}} \right]. \quad (5.6)$$

Using the completeness relation

$$\delta_{\mathbf{k}\mathbf{q}} = \frac{1}{N} \sum_{\mathbf{R}} e^{i(\mathbf{k}-\mathbf{q})\mathbf{R}} \quad (5.7)$$

where $\delta_{\mathbf{k}\mathbf{q}}$ is the Kronecker-Delta, we obtain

$$\begin{aligned} H &= - \sum_{\mathbf{k}} \sum_{i=1}^3 \left[t_i e^{-i\mathbf{k}\boldsymbol{\delta}_i} b_{\mathbf{k}}^\dagger a_{\mathbf{k}} + t_i e^{i\mathbf{k}\boldsymbol{\delta}_i} a_{\mathbf{k}}^\dagger b_{\mathbf{k}} \right] \\ &= - \sum_{\mathbf{k}} \sum_{i=1}^3 \begin{pmatrix} a_{\mathbf{k}}^\dagger & b_{\mathbf{k}}^\dagger \end{pmatrix} \begin{pmatrix} 0 & t_i e^{i\mathbf{k}\boldsymbol{\delta}_i} \\ t_i e^{-i\mathbf{k}\boldsymbol{\delta}_i} & 0 \end{pmatrix} \begin{pmatrix} a_{\mathbf{k}} \\ b_{\mathbf{k}} \end{pmatrix}. \end{aligned} \quad (5.8)$$

We define the matrix as

$$h(\mathbf{k}) = \begin{pmatrix} 0 & -t_1 e^{i\mathbf{k}\boldsymbol{\delta}_1} - t_2 e^{i\mathbf{k}\boldsymbol{\delta}_2} - t_3 e^{i\mathbf{k}\boldsymbol{\delta}_3} \\ -t_1 e^{-i\mathbf{k}\boldsymbol{\delta}_1} - t_2 e^{-i\mathbf{k}\boldsymbol{\delta}_2} - t_3 e^{-i\mathbf{k}\boldsymbol{\delta}_3} & 0 \end{pmatrix}. \quad (5.9)$$

Let us now consider the reciprocal lattice $\mathbf{G} = k\mathbf{b}_1 + l\mathbf{b}_2$ spanned by the reciprocal lattice vectors defined in (5.2) with k and l being integers. We notice that $h(\mathbf{k})$ is not periodic with respect to translation on the reciprocal lattice, i.e. $h(\mathbf{k} + \mathbf{G}) \neq h(\mathbf{k})$. For this to be the case, we need to fulfill the condition that $\mathbf{b}_i \boldsymbol{\delta}_j = 2\pi \delta_{ij}$.

Since we know that the difference between two bond vectors must yield a lattice vector in \mathbf{R} again, which does fulfill this condition, we perform a $U(1)$ gauge transform on the A site annihilation and creation operators:

$$a_{\mathbf{k}} \rightarrow e^{i\mathbf{k}\boldsymbol{\delta}_3} a_{\mathbf{k}}, \quad a_{\mathbf{k}}^\dagger \rightarrow e^{-i\mathbf{k}\boldsymbol{\delta}_3} a_{\mathbf{k}}^\dagger \quad (5.10)$$

In this new gauge the matrix becomes

$$h'(\mathbf{k}) = \begin{pmatrix} 0 & -t_1 e^{i\mathbf{k}(\boldsymbol{\delta}_1 - \boldsymbol{\delta}_3)} - t_2 e^{i\mathbf{k}(\boldsymbol{\delta}_2 - \boldsymbol{\delta}_3)} - t_3 \\ -t_1 e^{-i\mathbf{k}(\boldsymbol{\delta}_1 - \boldsymbol{\delta}_3)} - t_2 e^{-i\mathbf{k}(\boldsymbol{\delta}_2 - \boldsymbol{\delta}_3)} - t_3 & 0 \end{pmatrix}. \quad (5.11)$$

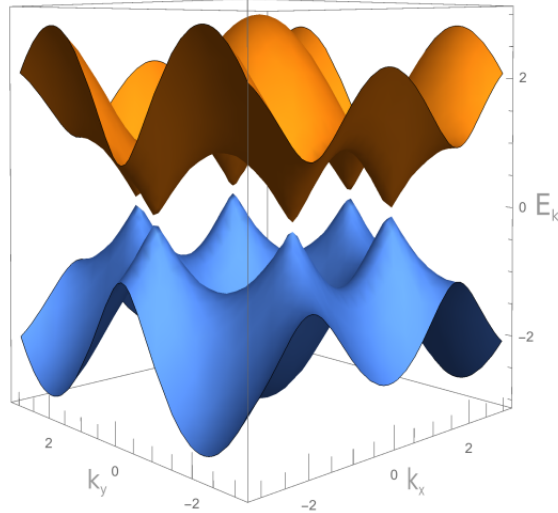


Fig. 5.2: Three-dimensional plot of graphene's semimetallic energy spectrum in \mathbf{k} -space for $a_0 = 1$ and $t = 1$. At \mathbf{K} and \mathbf{K}' the bands form *Dirac cones* around which the dispersion is linear.

Combining (5.1) and (5.3) we see that $\delta_i - \delta_3 = \mathbf{a}_i$ and therefore

$$h'(\mathbf{k}) = \begin{pmatrix} 0 & -t_1 e^{i\mathbf{k}\mathbf{a}_1} - t_2 e^{i\mathbf{k}\mathbf{a}_2} - t_3 \\ -t_1 e^{-i\mathbf{k}\mathbf{a}_1} - t_2 e^{-i\mathbf{k}\mathbf{a}_2} - t_3 & 0 \end{pmatrix} \quad (5.12)$$

which is finally invariant under lattice translations with $h'(\mathbf{k} + \mathbf{G}) = h'(\mathbf{k})$.

For the isotropic case $t_1 = t_2 = t_3$, we get

$$E = \pm t \sqrt{3 + 2 \cos \sqrt{3} a_0 k_y + 4 \cos \frac{\sqrt{3}}{2} a_0 k_y \times \cos \frac{3}{2} a_0 k_x}. \quad (5.13)$$

5.1.2 Massless Dirac Fermions

In Fig. 5.2 we see that the bands touch at the \mathbf{K} -points (see Fig. 5.1b). The reciprocal coordinates of these points are given by

$$\mathbf{K} = \frac{2\pi}{3a_0} \begin{pmatrix} 1 \\ \frac{1}{\sqrt{3}} \end{pmatrix}, \quad \mathbf{K}' = \frac{2\pi}{3a_0} \begin{pmatrix} 1 \\ -\frac{1}{\sqrt{3}} \end{pmatrix}. \quad (5.14)$$

At these so-called *Dirac cones* or *Dirac nodes* the dispersion becomes linear. Thus, let us expand $h'(\mathbf{k})$ around \mathbf{K} . Obviously, the matrix elements of $h'(\mathbf{k})$ become zero at $\mathbf{k} = \mathbf{K}$. Defining $\mathbf{q} = \mathbf{k} - \mathbf{K}$, for the first order term, we get

$$\begin{aligned} h'_{12}(\mathbf{k}) &= \left. \frac{\partial h'_{12}(\mathbf{k})}{\partial k_x} \right|_{\mathbf{k}=\mathbf{K}} (k_x - K_x) + \left. \frac{\partial h'_{12}(\mathbf{k})}{\partial k_y} \right|_{\mathbf{k}=\mathbf{K}} (k_y - K_y) \\ &= -\frac{3a_0}{2} (q_x - iq_y) \\ \Rightarrow \quad h''(\mathbf{q}) &= c \mathbf{q} \cdot \boldsymbol{\sigma} + \mathcal{O}(\mathbf{q}^2) \end{aligned} \quad (5.15)$$

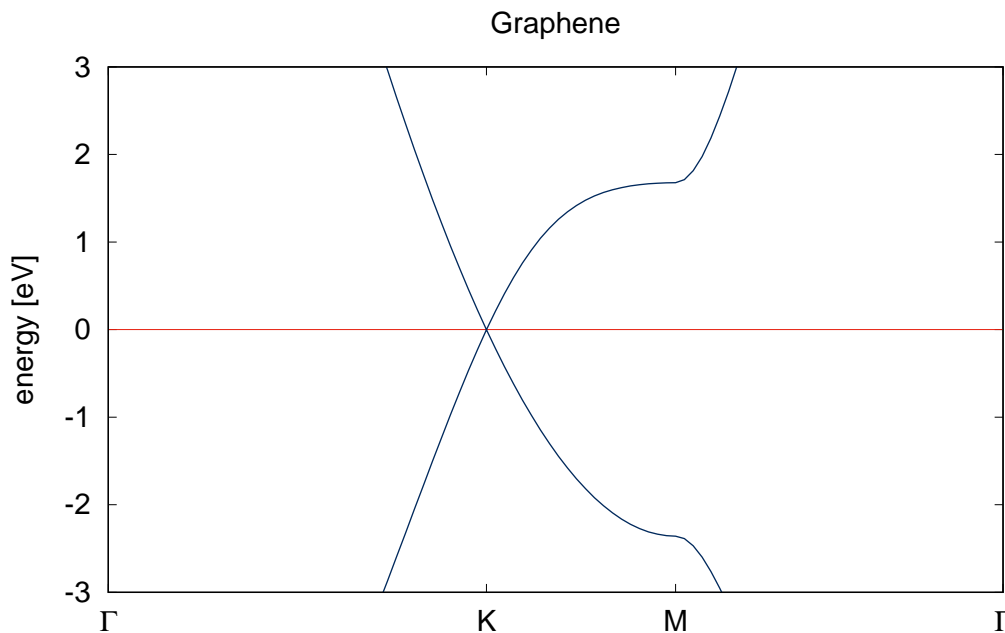


Fig. 5.3: Band structure of an infinitely extended sheet of graphene obtained with DFT. At the K -point the conduction and valence band meet, just as predicted by (5.13).

Above, we absorbed any prefactors into the constant c and defined $\boldsymbol{\sigma}$ to be the 2D vector that contains the first two Pauli matrices $\boldsymbol{\sigma} = (\sigma_x, \sigma_y)^\top$.

The electrons close to the \mathbf{K} -points are called *massless* Dirac Fermions, since the equation derived above resembles the Dirac equation of a free Fermion with mass $m = 0$.

5.1.3 DFT calculations for graphene

In this section the electronic structure of graphene obtained through DFT calculations is presented. Because WIEN2k accepts only three-dimensional structures as input, the unit cell has been chosen such that the layers of graphene are separated by a distance of 15\AA , thereby eliminating possible interactions along a third spatial dimension.

The bands given in Fig. 5.3 confirm the analytical results from (5.13). The conduction and valence band touch at the K -point and disperse linearly around it, forming the aforementioned Dirac cone. Having only a small band overlap, graphene classifies as a semimetal.

5.2 Symmetries

The two most important symmetries present in a sheet of graphene are inversion and time-reversal symmetry. In the case of real and isotropic hopping ($t_1 = t_2 = t_3$ and $\text{Im}(t_i) = 0$, $i \in 1, 2$) both are present. Next the consequences of these symmetries will be

analyzed.

A third symmetry of graphene, the C_3 symmetry, will not be part of our discussion. It can be shown, though, that the C_3 symmetry in combination with inversion and time-reversal symmetry fixes the position of the Dirac cones within the Brillouin zone [23].

Take notice that $h''(\mathbf{q})$ will be denoted as just $h(\mathbf{q})$ and we will drop the constant factor c from now on.

5.2.1 Inversion symmetry

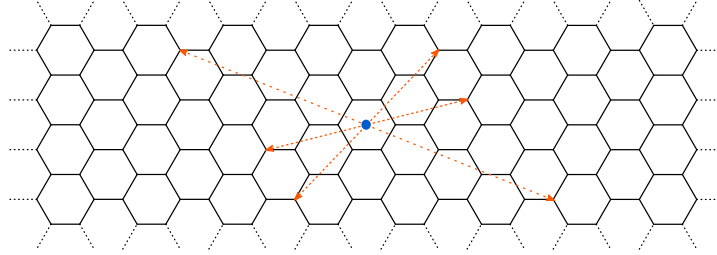


Fig. 5.4: An infinite sheet of graphene and an arbitrarily chosen inversion center (blue circle) that connects any two sites of the lattice (orange arrows).

The inversion operator I must be a unitary operator that flips the sign of the spatial variables of our system:

$$I : (x, y) \rightarrow (-x, -y) \quad (5.16)$$

Here, the matrix representation of the inversion operator is the first Pauli matrix σ_x . It can be easily shown that if the system is symmetric under inversion, i.e. $[H, I] = 0$, $h(\mathbf{q})$ must fulfill

$$h(\mathbf{q}) = \sigma_x h(-\mathbf{q}) \sigma_x. \quad (5.17)$$

Trivially, at $\mathbf{k} = \mathbf{K} \Rightarrow \mathbf{q} = 0$, adding a mass term and thereby opening a gap does not conflict with the condition above. Thus, inversion symmetry on its own does not protect the system's gaplessness.

5.2.2 Time-reversal symmetry

Time reversal has already been presented in section 2.3.1. As a reminder:

T inverts the direction of time

$$T : t \rightarrow -t \quad (5.18)$$

and for spinless systems we have identified T as the complex conjugate operator K . Thus, a time-reversal-invariant system behaves as

$$Th(\mathbf{q})T^{-1} = h(-\mathbf{q}). \quad (5.19)$$

5.2.3 Symmetry protection of the Dirac points

In the previous two sections we argued that neither inversion nor time-reversal symmetry protects the system from opening a gap. Let us now examine the combined effect of these symmetries.

Using (5.17) and (5.19), we can state that a system that is invariant under time reversal and inversion must conform to

$$TI h(\mathbf{q}) (TI)^{-1} = \sigma_x h^*(\mathbf{q}) \sigma_x = h^*(-\mathbf{q}) = h(\mathbf{q}). \quad (5.20)$$

In order to open a gap, let us add a mass term of the form $m\sigma_z$ to our Hamiltonian:

$$h(\mathbf{q}) = q_x \sigma_x + q_y \sigma_y + m \sigma_z \quad (5.21)$$

Demanding inversion and time-reversal symmetry, we get

$$\begin{aligned} h(\mathbf{q}) &= q_x \sigma_x + q_y \sigma_y + m \sigma_z \\ &= \sigma_x (q_x \sigma_x + q_y \sigma_y + m \sigma_z)^* \sigma_x = q_x \sigma_x + q_y \sigma_y - m \sigma_z \\ \Rightarrow \quad m \sigma_z &= -m \sigma_z \\ \Rightarrow \quad m &= 0 \end{aligned} \quad (5.22)$$

As such, there can be no gap in the presence of inversion and time-reversal symmetry. Although it is not forbidden to add any σ_x - or σ_y -terms, these perturbations would only result in shifting the nodes in reciprocal space.

As it has already been mentioned, the position of the Dirac cones can be fixed by requiring C_3 symmetry.

5.3 Topological properties

In chapter 2 the concepts of topological band theory were introduced. Let us now calculate the Berry phase of graphene to gain insight into its topological properties.

5.3.1 Berry phase of graphene

Suspecting the more interesting properties of our system around the Dirac Points, we first have a look at our Dirac Hamiltonian given by (5.15)

$$h(\mathbf{q}) = \mathbf{q} \cdot \boldsymbol{\sigma}. \quad (5.23)$$

It should be pointed out that we still denote $h''(\mathbf{q})$ as just $h(\mathbf{q})$ and that the constant factor c has been dropped. In polar coordinates \mathbf{q} and $h(\mathbf{q})$ read

$$\mathbf{q} = q \begin{pmatrix} \cos \varphi \\ \sin \varphi \end{pmatrix} \quad \text{with} \quad |\mathbf{q}| = q \quad (5.24)$$

$$h(\mathbf{q}) = q \begin{pmatrix} 0 & \cos \varphi - i \sin \varphi \\ \cos \varphi + i \sin \varphi & 0 \end{pmatrix} = q \begin{pmatrix} 0 & e^{-i\varphi} \\ e^{i\varphi} & 0 \end{pmatrix}. \quad (5.25)$$

The normalized eigenvectors of $h(\mathbf{q})$ are

$$|\psi_{-}\rangle = \frac{1}{\sqrt{2}} \begin{pmatrix} -e^{-i\varphi} \\ 1 \end{pmatrix} \quad \text{and} \quad |\psi_{+}\rangle = \frac{1}{\sqrt{2}} \begin{pmatrix} e^{-i\varphi} \\ 1 \end{pmatrix}. \quad (5.26)$$

We now use (2.9) to calculate the Berry connection. Let us remind ourselves that only the filled bands are taken into account. Thus, we will consider only $|\psi_{-}\rangle$.

$$\mathcal{A} = i \langle \psi_{-} | \nabla_{\mathbf{q}} | \psi_{-} \rangle \quad (5.27)$$

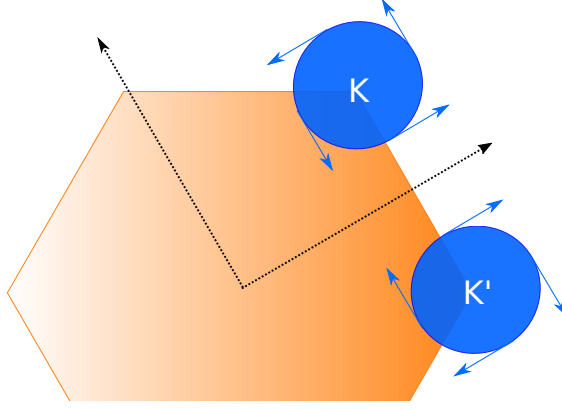


Fig. 5.5: Berry phase around the two Dirac nodes at \mathbf{K} and \mathbf{K}' is the winding number multiplied by π . The two nodes carry opposite vorticities $+1$ and -1 and introduce a measure of *topological charge*.

Because $|\psi_{-}\rangle$ does not depend on q and the gradient $\nabla_{\mathbf{q}}$ in polar coordinates is given by $\nabla_{\mathbf{q}} = (\frac{\partial}{\partial q}, \frac{1}{q} \frac{\partial}{\partial \varphi})^{\top}$, we obtain

$$\begin{aligned} \mathcal{A} &= \frac{i}{2} \begin{pmatrix} -e^{i\varphi} & 1 \end{pmatrix} \frac{1}{q} \frac{\partial}{\partial \varphi} \begin{pmatrix} -e^{-i\varphi} \\ 1 \end{pmatrix} \\ &= \frac{i^2}{2q} \begin{pmatrix} -e^{i\varphi} & 1 \end{pmatrix} \begin{pmatrix} e^{-i\varphi} \\ 0 \end{pmatrix} \\ &= \frac{1}{2q} \end{aligned} \quad (5.28)$$

With (2.7), we are able to derive the wave function's Berry phase. For our loop \mathcal{C} , we choose only a small circle around the \mathbf{K} -point, as we are only interested in the Berry phase for transport around the Dirac cone at $\mathbf{k} = \mathbf{K}$ for now.

$$\gamma = \int_{\mathcal{C}} d\mathbf{q} \mathcal{A} = \int_0^{2\pi} d\varphi q \mathcal{A} = \pi \quad (5.29)$$

Analogously, it can be shown that the Dirac fermion sitting at \mathbf{K}' carries a Berry phase of $\gamma = -\pi$, so for the whole Brillouin zone, the Berry phase amounts to $\gamma = 0$.

Accordingly, the Chern number must be $C = 0$ as well. This certainly does not come as a surprise, since we have already shown that the Chern number C must vanish for time-reversal-invariant systems in (2.19).

We see that the Berry phase around the \mathbf{K} -points is nothing but the winding number multiplied by π , which is then either $+1$ or -1 . This introduces a measure of *topological charge* for the Dirac points in k -space, which tells us how the wave functions wind around these singular points differently with respect to each other. The \mathbf{K} -point that carries the topological charge $+1$ is called a vortex, whereas the other one is called an anti-vortex (see Fig. 5.5).

Them coming together and annihilating each other would result in a gap, but as long as C_3 symmetry is present, the vortices are fixed.

5.3.2 Breaking inversion symmetry

Breaking inversion symmetry will result in a gapped spectrum. This can easily be done by adding a mass term to the Hamiltonian $h(\mathbf{q})$:

$$h_{gap}(\mathbf{q}) = h(\mathbf{q}) + m\sigma_z \quad (5.30)$$

Going through the same calculations as above results in a Berry phase γ which picks up a contribution that is proportional to $(1 - m)$.

This means, upon opening a gap, the Berry phase will not vanish instantly, but will decrease progressively with an increasing gap, whereas for $m \rightarrow 0$ we return to the case considered previously.

As adding a term proportional to σ_z does not violate time-reversal symmetry, the Chern number is still zero and the system can not enter a quantum Hall phase.

5.3.3 Breaking time-reversal symmetry and the Haldane model

In the previous section it was shown that breaking inversion symmetry does not do the job if we want to observe interesting, topological phenomena, like the quantum Hall effect.

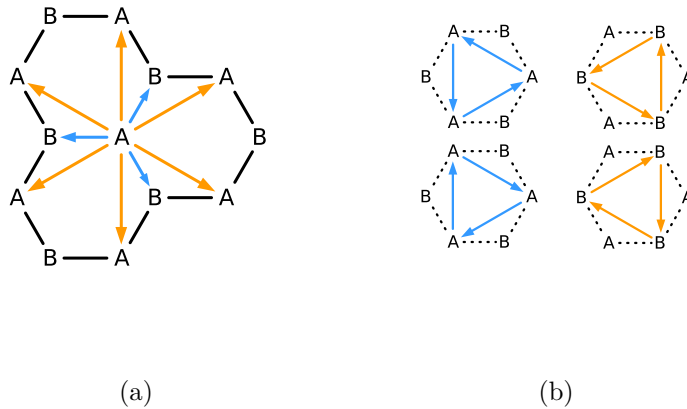


Fig. 5.6: (a) nearest-neighbor (blue) and next-nearest-neighbor, hopping bonds $\tilde{\delta}_1, \tilde{\delta}_2, \tilde{\delta}_3, \tilde{\delta}_4, \tilde{\delta}_5, \tilde{\delta}_6$, (orange); (b) different directions of rotation for next-nearest-neighbor hopping for sublattices A and B.

Of course, we could apply an extrinsic magnetic field, which breaks time-reversal symmetry, but preferably we would like to keep the translation invariance of our system intact and we are more involved in finding intrinsic effects, i.e. properties of graphene that are not field-induced anyway.

Duncan Haldane was the first who managed to mimic the integer quantum Hall effect on a honeycomb lattice [30].

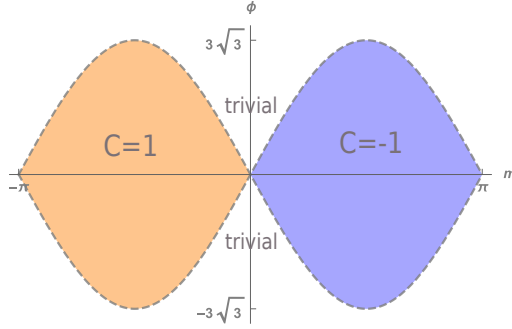


Fig. 5.7: Haldane phase diagram. Depending on magnitude of the inversion-symmetry-breaking term $m\sigma_z$ and the phase ϕ , the Haldane model assumes different quantum Hall phases corresponding to different Chern numbers C . In the orange region $C = 1$ and in the blue region $C = -1$. Everywhere else the system's topology is trivial.

Starting at our real-space Hamiltonian (5.4) and assuming isotropic hopping $t = t_1 = t_2 = t_3$, we now add a next-nearest-neighbor hopping term along the next-nearest neighbor bonds $\tilde{\delta}_i$ (see Fig. 5.6a):

$$\begin{aligned}
 H_{Hal.} = & - \sum_{\mathbf{R}} \sum_{i=1}^3 t \left[b^\dagger(\mathbf{R} + \delta_i) a(\mathbf{R}) + a^\dagger(\mathbf{R}) b(\mathbf{R} + \delta_i) \right] \\
 & - \sum_{\mathbf{R}} \sum_{i=1}^3 t' \left[e^{i\phi} a^\dagger(\mathbf{R} + \tilde{\delta}_i) a(\mathbf{R}) + e^{-i\phi} b^\dagger(\mathbf{R} + \tilde{\delta}_i) b(\mathbf{R}) \right] + \text{h.c.} \\
 & + m \left[\sum_{\mathbf{R}_A} a^\dagger(\mathbf{R}_A) a(\mathbf{R}_A) - \sum_{\mathbf{R}_B} b^\dagger(\mathbf{R}_A) b(\mathbf{R}_A) \right]
 \end{aligned} \tag{5.31}$$

The crucial point is that we do not restrict the next-nearest-neighbor hopping term t' to be real, as we do for t . In fact, t' is completely imaginary. This leads to the time-reversal symmetry being broken, as this term will change sign if T is applied.

Additionally, we have broken inversion symmetry by adding a mass term, which is the third line of the equation above.

In k -space representation, this Hamiltonian takes a much shorter form:

$$h_{Hal.} = h_0(\mathbf{q}) + m\sigma_z + 2t' \sum_{i=1}^6 \sigma_z \sin \mathbf{k} \cdot \tilde{\delta}_i \tag{5.32}$$

The first addend $h_0(\mathbf{k})$ is the unexpanded Hamiltonian, previously called $h'(\mathbf{k})$ in (5.12). It can be shown that the Chern number C can take three possible values: $-1, 0$ and 1 [30]. Which topological phase the system assumes, depends on the values of the phase ϕ and the inversion-symmetry breaking term m .

The interplay of ϕ and m results in the famous Haldane phase diagram (see Fig. 5.7). For graphene, such a behavior has not been observed. Nevertheless, such a system has been realized experimentally for a system of ultracold fermions [33].

6 \mathbb{Z}_2 invariant

In the previous chapter, we thoroughly examined the electronic and topological properties of a sheet of graphene. We found that graphene features two linearly dispersing Dirac cones in its Brillouin zone, at which the bands touch. The gaplessness of the system is protected by inversion and time-reversal symmetry, whereas the cone's position is fixed by C_3 symmetry.

We learned that if we want to find a non-zero Hall conductance, time-reversal symmetry has to be broken. This can be accomplished by either applying a magnetic field, or by introducing complex hopping. The competition between the inversion- and the time-reversal-breaking term finally resulted in the Haldane phase diagram (see Fig. 5.7).

Since spin-orbit coupling in graphene is weak, only small effects of complex hopping have been observed yet. This might lead to believe that, in the end, graphene does not exhibit any interesting topological behavior at all. Kane and Mele first realized that systems with intact time-reversal symmetry can enter an exotic topological phase too [34]. This new phase of matter is called the Quantum Spin Hall phase and it hosts edge states that are not transporting charge, as in the case for the Hall conductance, but it features counterpropagating edge modes that carry *spin charge* (see Fig. 6.1). The topological invariant related to this effect is called the \mathbb{Z}_2 invariant [29]. In two dimensions it is given by

$$(-1)^{\mathbb{Z}_2} = \prod_{i=1}^4 \frac{\sqrt{\det[A(\Lambda_i)]}}{\text{Pf}[A(\Lambda_i)]}. \quad (6.1)$$

The matrix elements $A_{nm}(\mathbf{k})$ above are defined as

$$A_{nm}(\mathbf{k}) = \langle u_{-\mathbf{k}}^n | T | u_{\mathbf{k}}^m \rangle \quad (6.2)$$

and Λ_i are the points in the Brillouin zone of a spin system which stay invariant under time reversal. Let us remind ourselves that the time-reversal operator T does not only flip the sign of the crystal momentum k , but also of the spin. Considering a spinless system, every k -point of the Brillouin zone would be a time-reversal-invariant momentum

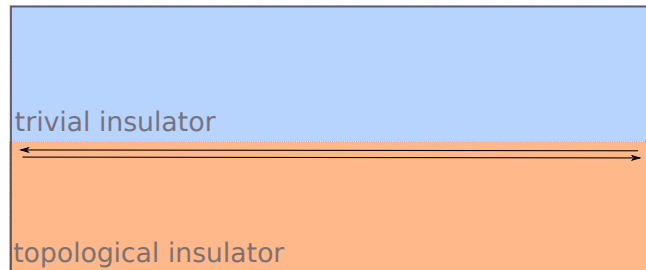


Fig. 6.1: Interface between two insulators with different topologies resulting in spin-polarized, counterpropagating edge modes.

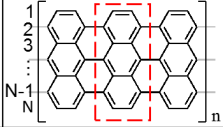
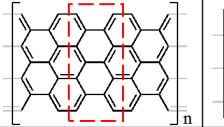
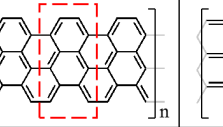
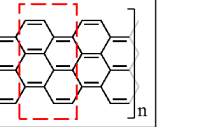
Termination type	Zigzag ($N = \text{Odd}$)	Zigzag' ($N = \text{Odd}$)	Zigzag ($N = \text{Even}$)	Bearded ($N = \text{Even}$)
Unit cell shape				
Bulk Symmetry	Inversion/mirror	Inversion/mirror	Mirror	Inversion
\mathbb{Z}_2	$\frac{1 + (-1)^{\lfloor \frac{N}{3} \rfloor + \lfloor \frac{N+1}{2} \rfloor}}{2}$	$\frac{1 - (-1)^{\lfloor \frac{N}{3} \rfloor + \lfloor \frac{N+1}{2} \rfloor}}{2}$		$\frac{1 - (-1)^{\lfloor \frac{N}{3} \rfloor}}{2}$

Fig. 6.2: Categorization of the different armchair graphene nanoribbons (AGNR). The unit cell is given in red and the brackets denote a specific termination of an effectively infinitely long AGNR. The hydrogen atoms saturating the structures are omitted. The width N is given by the number of carbon atoms in one dimer along the lateral direction. The floor function $\lfloor x \rfloor$ outputs x if x is an integer and otherwise the next lower integer [5].

(TRIM) because we know by Kramers' theorem that for every energy of an eigenstate $|\mathbf{k}\rangle$, the time-reversed state $T|\mathbf{k}\rangle$ has the same energy, as long H and T commute.

The \mathbb{Z}_2 invariant can be tricky to calculate, since it requires you to find a smooth gauge over the whole Brillouin zone. Other methods to obtain the invariant have been introduced, one of which is only applicable for inversion-symmetric systems. As the structures examined in the next chapter preserve inversion symmetry, we will choose this approach accordingly.

Fu and Kane were able to show that if $[H, IT] = 0$ is obeyed, the Pfaffian can be expressed through the eigenvalues of the inversion operator [28]

$$\text{Pf}[A]^2 = \prod_{i=1}^N \zeta_i. \quad (6.3)$$

This drastically simplifies the calculation of the \mathbb{Z}_2 invariant because the eigenvalues of the inversion operator I can be obtained much more easily than a global gauge. It might seem strange that although this classification is used for spinful systems, no spin dependent term appears in (6.3) at all. Of course, bands have inversion eigenvalues, irrespective of whether spin is considered or not. Here, spin-orbit coupling's role is to ensure that an energy gap exists and is finite everywhere.

In Fig. 6.2 the \mathbb{Z}_2 invariants for armchair graphene nanoribbons (AGNR) of different width, termination and unit cells are given.

To characterize the topology of the quasi-1D AGNR, we calculate the Zak phase ϕ^Z , which is just the one-dimensional Berry phase [49]. It reads

$$\phi_n^Z = i \int_{-\pi}^{\pi} dk \langle u_k^n | \partial_k | u_k^n \rangle. \quad (6.4)$$

Due to the spatial symmetries of the system, the intercell Zak phase of a system is quantized at either 0 or π . The \mathbb{Z}_2 invariant and the sum of all intercell Zak phases ϕ_n^Z

are related through

$$(-1)^{\mathbb{Z}_2} = \exp\left(i \sum_n \phi_n^Z\right). \quad (6.5)$$

This classification enables us to predict when interface states at the heterojunctions between different AGNR should arise due to the gap closing at the transition from the topologically trivial to the non-trivial material. In this way we hope to construct AGNR with new, topological bands that are induced by the coupling of these interface states.

7 Su-Schrieffer-Heeger model

This chapter is devoted to the topological properties of the one-dimensional, organic polymer called polyacetylene. It consists of a chain of carbon atoms with alternating single and double bonds between them, each with one hydrogen atom (see Fig. 7.1). In 1979 Su, Schrieffer and Heeger (SSH) proposed a tight-binding model for such a system and it is introduced to explain the origin of certain bands in the spectrum of graphene-nanoribbon composites later on.

7.1 Tight-binding of polyacetylene

The model Hamiltonian for a N unit cell chain, with each cell consisting of two sublattices A and B , is given in terms of single particle creation and annihilation operators that act on either the A or B sublattice (see Fig. 7.1).

$$H = - \sum_{n=1}^N t_1 b_n^\dagger a_n - \sum_{n=1}^{N-1} t_2 a_{n+1}^\dagger b_n + h.c. \quad (7.1)$$

Here, a_n is the annihilation operator of an electron on the n^{th} site of sublattice A and b_n the annihilation operator of one on the n^{th} site of sublattice B . While t_1 represents the intracell hopping, meaning the hopping along a double bond, t_2 is for intercell hopping along a single bond.

Let l_0 be the spatial distance between two atoms belonging to the same sublattice. The Fourier transform of these operators is given by

$$a_n = \frac{1}{N} \sum_k e^{iknl_0} a_k \quad (7.2)$$

$$a_n^\dagger = \frac{1}{N} \sum_k e^{-iknl_0} a_k \quad (7.3)$$

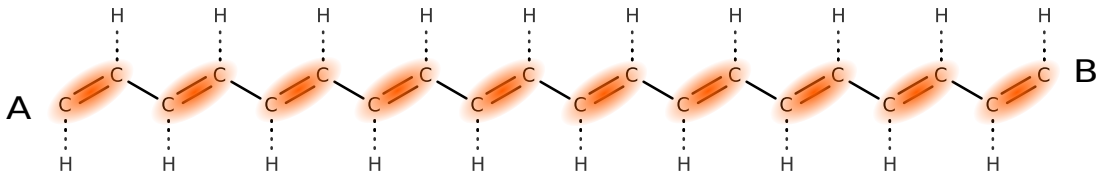


Fig. 7.1: Structural diagram of polyacetylene in its trans configuration. The unit cells are marked in red. The lower row of carbon atoms represents the A sublattice, whereas the upper row atoms sit on the B sublattice.

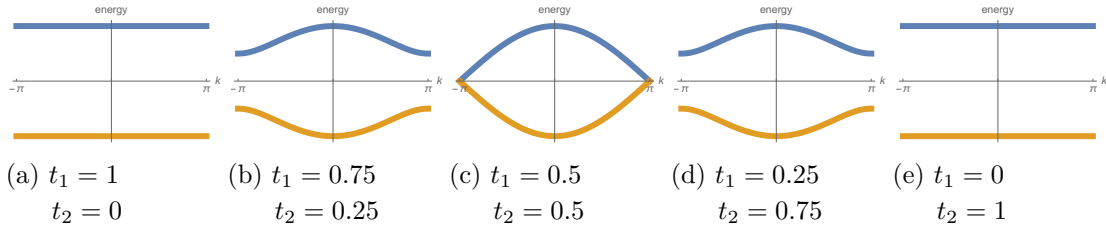


Fig. 7.2: Dispersion in polyacetylene for different hopping amplitudes at $l_0 = 1$. (a), (b), (d) and (e) for staggered hopping amplitudes $t_1 \neq t_2$ we find an insulating phase; (c) gap is closed at the boundaries of the Brillouin zone which renders the material semimetallic.

Considering periodic boundary conditions, the Fourier transformed Hamiltonian is given by

$$H = - \sum_{n=1}^N \sum_{k,q} t_1 \frac{1}{N} e^{i(k-q)l_0 n} \left[b_q^\dagger a_k - a_q^\dagger b_k \right] - \sum_{n=1}^N \sum_{k,q} t_2 \frac{1}{N} e^{i(k-q)l_0 n} \left[e^{-iq l_0} a_q^\dagger b_k + e^{ik l_0} b_q^\dagger a_k \right]. \quad (7.4)$$

In the thermodynamic limit $N \rightarrow \infty$, we can use the completeness relation

$$\delta_{kq} = \frac{1}{N} \sum_{n=1}^{\infty} e^{i(k-q)nl_0} \quad (7.5)$$

which leads to

$$H = - \sum_k t_1 \left[b_q^\dagger a_k + a_q^\dagger b_k \right] - \sum_k t_2 \left[e^{-ikl_0} a_q^\dagger b_k + e^{ikl_0} b_q^\dagger a_k \right] \quad (7.6)$$

$$= - \sum_k \begin{pmatrix} a_k^\dagger & b_k^\dagger \end{pmatrix} \begin{pmatrix} 0 & t_1 + t_2 e^{-ikl_0} \\ t_1 + t_2 e^{+ikl_0} & 0 \end{pmatrix} \begin{pmatrix} a_k \\ b_k \end{pmatrix}. \quad (7.7)$$

Let us define

$$h(k) = - \begin{pmatrix} 0 & t_1 + t_2 e^{-ikl_0} \\ t_1 + t_2 e^{+ikl_0} & 0 \end{pmatrix}. \quad (7.8)$$

Diagonalizing $h(k)$, we obtain the energy eigenvalues

$$\begin{aligned} E^2 &= (t_1 + t_2 e^{-ikl_0})(t_1 + t_2 e^{+ikl_0}) \\ \Leftrightarrow E^2 &= t_1^2 + t_2^2 + t_1 t_2 (e^{+ikl_0} + e^{-ikl_0}) \\ \Leftrightarrow E &= \pm \sqrt{t_1^2 + t_2^2 + 2t_1 t_2 \cos kl_0} \end{aligned} \quad (7.9)$$

We notice that as long as $t_1 \neq t_2$ holds, the system is gapped, but for $t_1 = t_2$ (see Fig. 7.2c) this model describes a conductor. By Peierls' theorem we know that one-dimensional metals are not stable [51]. Therefore, we would expect to find such a system with staggered hopping amplitudes $t_1 \neq t_2$ in nature.

7.2 Topological properties of polyacetylene

Let us now investigate the system's behavior at $t_1 = t_2$, where the chain becomes metallic (see Fig. 7.2c). To this end, consider the matrix element $h_{12}(k)$ from (7.8):

$$h_{12}(k) = -t_1 - t_2 e^{-ikl_0} = -t_1 - t_2 \cos kl_0 + it_2 \sin kl_0 \quad (7.10)$$

Having split $h_{12}(k)$ in its real and imaginary part, we can easily write $h(k)$ as

$$h(k) = -\mathbf{g}(k) \cdot \boldsymbol{\sigma} = - \begin{pmatrix} t_1 + t_2 \cos kl_0 & t_2 \sin kl_0 \\ t_2 \sin kl_0 & t_1 - t_2 \cos kl_0 \end{pmatrix} \begin{pmatrix} \sigma_x \\ \sigma_y \end{pmatrix} \quad (7.11)$$

where we defined $\mathbf{g}(k) = \begin{pmatrix} t_1 + t_2 \cos kl_0 & t_2 \sin kl_0 \\ t_2 \sin kl_0 & t_1 - t_2 \cos kl_0 \end{pmatrix}$ and σ_i are the Pauli matrices. In its polar representation $\mathbf{g}(k)$ becomes

$$\mathbf{g}(k) = |\mathbf{g}(k)| \begin{pmatrix} \cos \phi(k) \\ \sin \phi(k) \end{pmatrix}. \quad (7.12)$$

As we are interested in how the vector $\mathbf{g}(k)$ winds around the Brillouin zone, let us solve for $\phi(k)$.

$$\begin{aligned} \frac{g_2(k)}{g_1(k)} &= \tan \phi(k) \quad \Leftrightarrow \quad \phi(k) = \arctan \frac{g_2(k)}{g_1(k)} \\ \phi(k) &= \arctan \frac{t_2 \sin kl_0}{t_1 + t_2 \cos kl_0} \end{aligned} \quad (7.13)$$

In Fig. 7.3 we see how the vector $\mathbf{g}(k)$ evolves through the first Brillouin zone for different hopping amplitudes t_1 and t_2 . t_1 acts as the position of the center of the sphere on the x -axis while t_2 determines its radius.

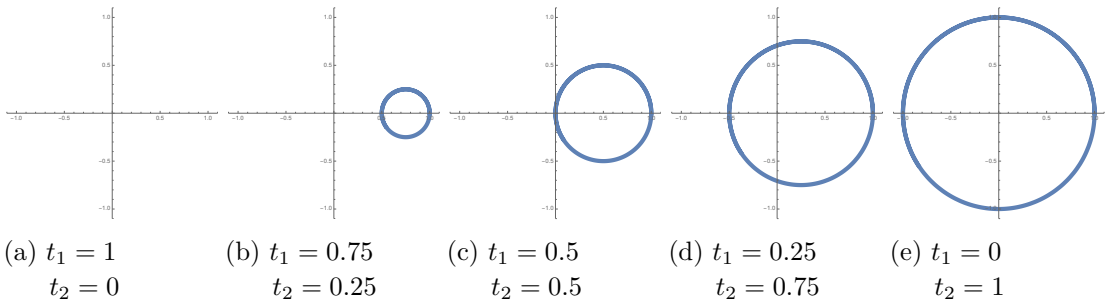


Fig. 7.3: Parametric plot of the vector $\mathbf{g}(k)$ for different hopping amplitudes. (a) $\mathbf{g}(k)$ traces out a circle with radius $R_{\mathbf{g}} = 0$ resulting in a point at $x = 1$; (c) at the phase transition the origin of the system and the closed loop touch; (d) system has entered a topological phase.

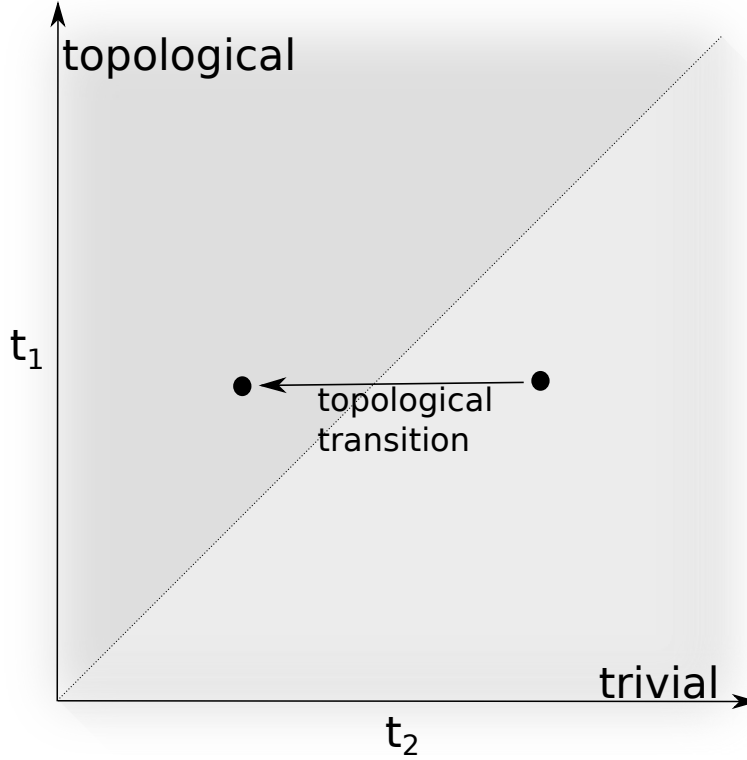


Fig. 7.4: Phase diagram of the topological phases of the system with respect to the hopping parameters t_1 and t_2 . Overstepping the boundary along $t_1 = t_2$ results in a topological phase transition.

Thus, the condition for $\mathbf{g}(k)$ to enclose the origin is

$$\frac{t_2}{t_1} > 1 \quad (7.14)$$

It can be shown easily that the winding number of the curve $\mathbf{g}(k)$ around the origin times π is nothing but the Zak phase ϕ^Z along the chain [52]. Therefore, it assumes either 0 or π as a value depending on whether the curve encloses the origin or not. Hence,

$$\begin{aligned} \phi^Z = 0 & \quad \text{for } \frac{t_2}{t_1} < 1, \\ \phi^Z = \pi & \quad \text{for } \frac{t_2}{t_1} > 1. \end{aligned} \quad (7.15)$$

Increasing t_2/t_1 , we see that at $t_2/t_1 = 1$ a topological phase transition takes place (see Fig. 7.4), characterized by a change of the Zak phase $\phi^Z = 0 \rightarrow \phi^Z = \pi$.

The global topology of the system in terms of the Zak phase thus solely depends on the ratio between inter- and intracell hopping.

7.3 SSH model for AGNR composites

As polyacetylene is not the material that we are ultimately interested in, let us use what we have learned so far on composites consisting of AGNR of different width, which is

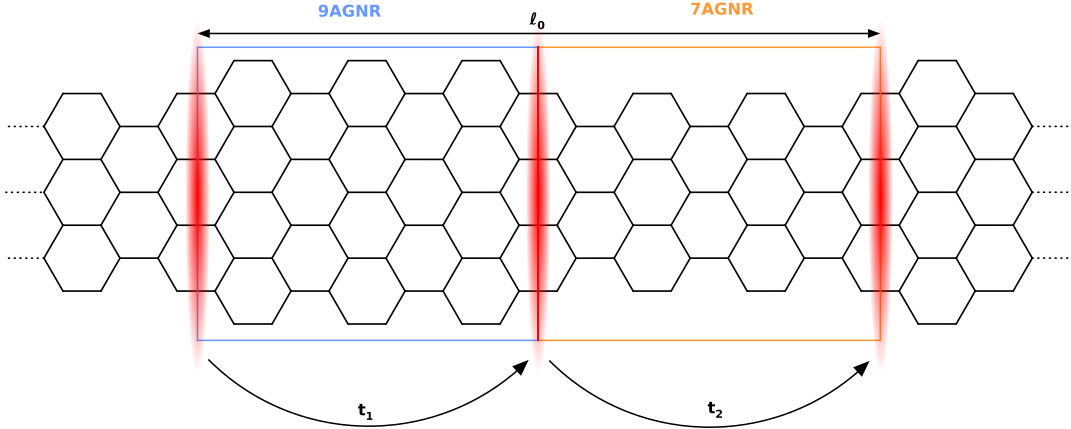


Fig. 7.5: AGNR composite that consists of a 9 atom wide and a 7 atom wide AGNR. Combined, the blue and the orange box represent the unit cell of this quasi-1D system with length l_0 . The edge states, which arise due to the different \mathbb{Z}_2 invariants of the components, are localized at the interfaces and are highlighted in red. The overlap between the interface states is given by t_1 for intracell and by t_2 for intercell hopping.

introduced in depth in chapter 8. For now, just assume a chain of alternating AGNR which are 7 and 9 carbon atoms wide (see Fig. 7.5).

With Fig. 6.2 we notice that these two AGNR have different \mathbb{Z}_2 invariants. As the band gap must be closed necessarily at the transition between materials in different topological phases, we expect edge states at the interfaces. It is our goal to describe the behavior of these states with the SSH model, so let us assume that the overlap between the interface states is given by the hopping amplitudes t_1 and t_2 . Joining the system's components to a supercell that contains two of these interfaces, the dispersion between the interfaces can be described analogously to the polyacetylene system.

Whether the global topology in terms of the Zak phase ϕ^Z of this effective chain is trivial or not depends on the ratio t_2/t_1 . Note, however, that we only consider the local topology of the system, meaning the value of the \mathbb{Z}_2 invariant of its components, as we are not interested in the edge states at the boundary of the chain, but rather assume an infinitely long chain and examine the consequences of the interplay between the topological interface states.

In [6], sinusoidally dispersing bands close to the Fermi level are interpreted to be the result of the coupling between interface states as described above. If these bands were the consequence of the overall topology of the system as claimed, one could easily alter the electronic properties of AGNR composites by tuning the overlap between these states. In the next chapter we find bands that exhibit such a dispersion in smaller structures and examine whether it is justified to associate them with topology.

8 Graphene nanoribbons

8.1 Different forms of graphene nanoribbons

Graphene nanoribbons (GNR) are thin strips of graphene. These quasi-1D systems exhibit different electronic and topological properties depending on their width, edge shape and unit cell termination. In general, any graphene nanoribbon can be generated by connecting dimers via a translation of a lattice vector.

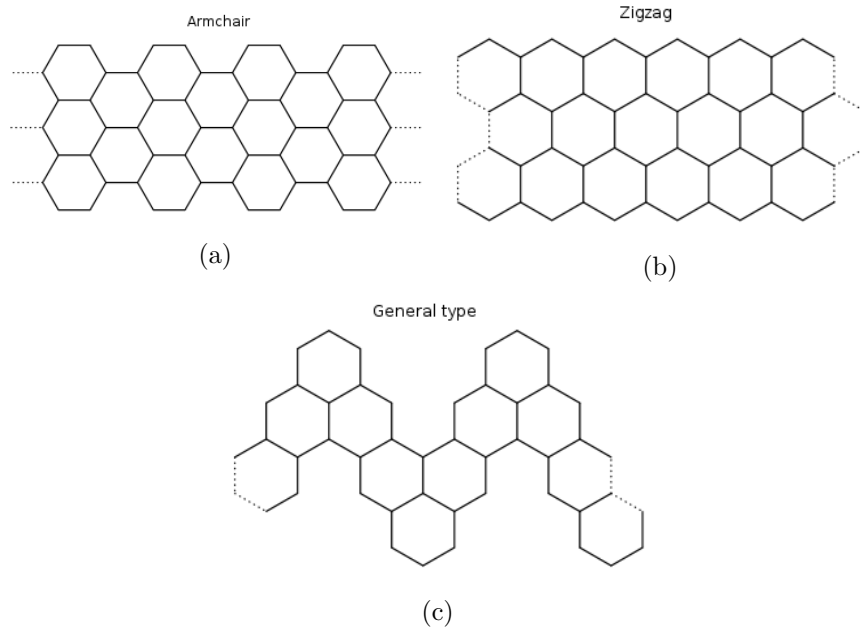


Fig. 8.1: Different types of graphene nanoribbons

In the following discussion, we are focussing on the armchair graphene nanoribbons (AGNR) (see Fig. 8.1a). Be aware that in order to avoid dangling bonds, we always consider hydrogen-saturated GNR for our DFT calculations. A carbon-hydrogen bond length of 1.06\AA has been chosen and the hydrogen atoms were placed at an angle of 90° for the pure 7 and 9AGNR, and at an angle of 120° to the longitudinal direction for the composite structures.

The next-neighbor distance of the carbon atoms has been adjusted to 1.4245\AA .

8.2 Tight-binding of AGNR of any width

Let us consider an infinitely long AGNR of width W and a unit cell of length A_0 . With Fig. 8.2 at hand we can easily construct the tight-binding Hamiltonian in real space

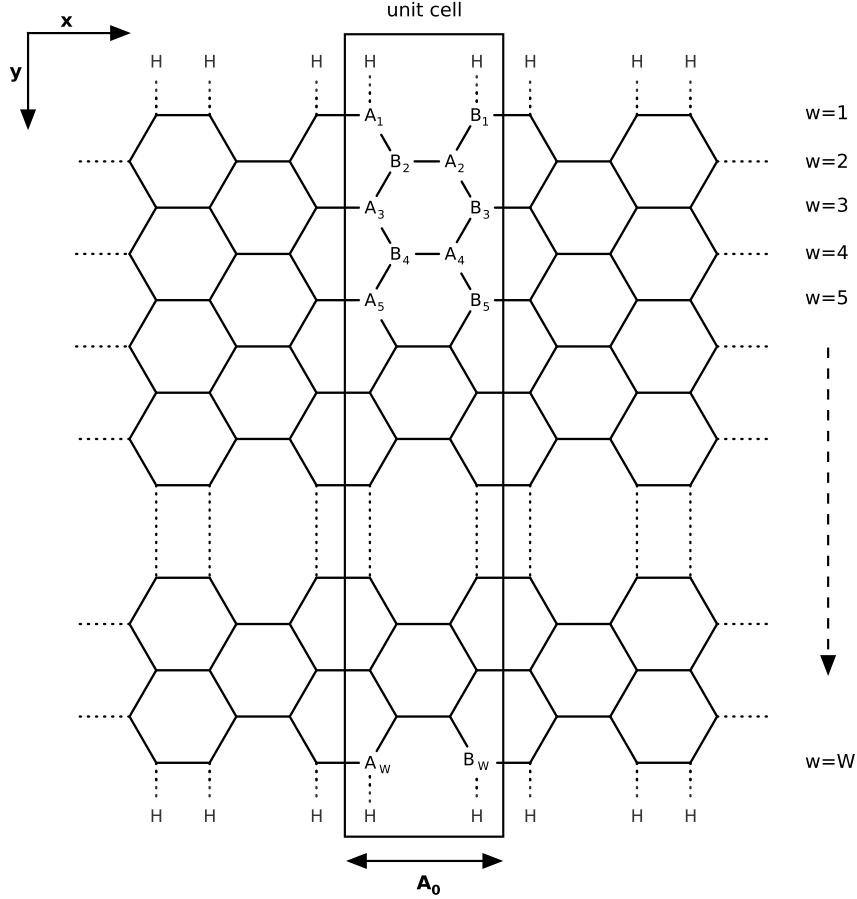


Fig. 8.2: AGNR of width W . We have periodic boundaries in the x -direction. The width of the AGNR is determined by the number of carbon atoms in the dimers it consists of. Each unit cell contains two such dimers with sublattices A and B .

regarding only nearest-neighbor hopping.

$$\begin{aligned}
 H = & -t \sum_n \left[\sum_{w \text{ odd}} a_n^\dagger(w) b_{n-1}(w) + \sum_{w \text{ even}} a_n^\dagger(w) b_n(w) + h.c. \right] \\
 & - t \sum_n \sum_w^{W-1} \left[a_n^\dagger(w+1) b_n(w) + b_n^\dagger(w+1) a_n(w) + h.c. \right] \quad (8.1)
 \end{aligned}$$

$a_n^\dagger(w)$ and $b_n^\dagger(w)$ are the creation operators that create an electron at the A_w and B_w site in the n^{th} unit cell while $a_n(w)$ and $b_n(w)$ are the corresponding annihilation operators. The upper line of this Hamiltonian describes longitudinal hopping along the x -direction, whereas the lower line represents transverse hopping along the width of the AGNR. Since we consider a system with a finite width W , but with periodic boundary conditions along the x -direction, we can Fourier transform the creation and annihilation operators

along that axis.

$$a_n^\dagger(w) = \frac{1}{L_x} \sum_k e^{-ikx_{n,A_w}} a_k(w) \quad (8.2)$$

$$b_n^\dagger(w) = \frac{1}{L_x} \sum_k e^{-ikx_{n,B_w}} b_k(w) \quad (8.3)$$

Here, k is the crystal momentum and x_{n,A_w} and x_{n,B_w} are the x -coordinates of the A_w and B_w sites in the n^{th} cell.

Let us now assume that the x -coordinate does only change for longitudinal hopping, so we get

$$x_{n,A_1} = x_{n,B_2} = x_{n,A_3} = \dots = x_n, \quad (8.4)$$

$$x_{n,B_1} = x_{n,A_2} = x_{n,B_3} = \dots = x_n + \frac{A_0}{2}. \quad (8.5)$$

with A_0 being the length of the unit cell (see Fig. 8.2).

The Fourier transform of one of the creation annihilation pairs reads

$$a_n^\dagger(w)b_{n-1}(w) = \frac{1}{L_x} \sum_{k,k'} e^{i(k-k')x_n} e^{-ik'\frac{A_0}{2}} a_{k'}^\dagger(w)b_k(w). \quad (8.6)$$

Using

$$\delta_{k,k'} = \frac{1}{L_x} \sum_n e^{i(k-k')x_n}, \quad (8.7)$$

we obtain the Fourier transform of (8.1) as

$$\begin{aligned} H = & -t \sum_k \left[\sum_{w \text{ odd}} e^{-ik\frac{A_0}{2}} a_k^\dagger(w)b_k(w) + \sum_{w \text{ even}} e^{-ik\frac{A_0}{2}} a_k^\dagger(w)b_k(w) + h.c. \right] \\ & - t \sum_k \sum_w^{W-1} \left[a_k^\dagger(w+1)b_k(w) + b_k^\dagger(w+1)a_k(w) + h.c. \right]. \end{aligned} \quad (8.8)$$

Since both longitudinal hoppings acquire the same phase factor, we can merge the sums and get

$$\begin{aligned} H = & -t \sum_k \sum_w^W \left[e^{-ik\frac{A_0}{2}} a_k^\dagger(w)b_k(w) + h.c. \right] \\ & - t \sum_k \sum_w^{W-1} \left[a_k^\dagger(w+1)b_k(w) + b_k^\dagger(w+1)a_k(w) + h.c. \right]. \end{aligned} \quad (8.9)$$

By adding and subtracting

$$a_k^\dagger(W+1)b_k(W) + b_k^\dagger(W+1)a_k(W) + h.c., \quad (8.10)$$

this expression can be transformed to

$$H = -t \sum_k \sum_w^W \left[e^{-ik\frac{A_0}{2}} a_k^\dagger(w)b_k(w) + a_k^\dagger(w+1)b_k(w) + b_k^\dagger(w+1)a_k(w) + h.c. \right] \quad (8.11)$$

$$+ t \sum_k \left[a_k^\dagger(W+1)b_k(W) + b_k^\dagger(W+1)a_k(W) + h.c. \right]. \quad (8.12)$$

The lower term of (8.12) will be omitted because it does not contribute to the energies as we will see later.

As an ansatz, we define the one-particle state

$$|\Psi(k)\rangle = |\psi_A(k)\rangle + |\psi_B(k)\rangle = \sum_w^W \left(\alpha_w a_k^\dagger(w) + \beta_w b_k^\dagger(w) \right) |0\rangle. \quad (8.13)$$

Inserting this into the Schrödinger equation

$$H |\Psi(k)\rangle = E |\Psi(k)\rangle \quad (8.14)$$

and using the anti-commutation relations

$$\left\{ a_k(w), a_{k'}^\dagger(w') \right\} = \delta_{k,k'} \delta_{w,w'}, \quad (8.15)$$

$$\left\{ b_k(w), b_{k'}^\dagger(w') \right\} = \delta_{k,k'} \delta_{w,w'}, \quad (8.16)$$

finally yields

$$E |\Psi(k)\rangle = -t \sum_w^W \left[e^{-ik\frac{A_0}{2}} \beta_w a_k^\dagger(w) + \beta_w a_k^\dagger(w+1) + \beta_{w+1} a_k^\dagger(w) + e^{+ik\frac{A_0}{2}} \alpha_w b_k^\dagger(w) + \alpha_w b_k^\dagger(w+1) + \alpha_{w+1} b_k^\dagger(w) \right] |0\rangle. \quad (8.17)$$

Shifting the sums and doing a coefficient comparison with $E |\Psi(k)\rangle$, we find the following equations of motion

$$E\alpha_w = -t \left(e^{-ik\frac{A_0}{2}} \beta_w + \beta_{w-1} + \beta_{w+1} \right), \quad (8.18)$$

$$E\beta_w = -t \left(e^{+ik\frac{A_0}{2}} \alpha_w + \alpha_{w-1} + \alpha_{w+1} \right). \quad (8.19)$$

As our system has a finite width, we want our amplitudes to vanish at $w = 0$ and $w = W + 1$ and thus we impose the boundary conditions

$$\alpha_0 = \beta_0 = \alpha_{W+1} = \beta_{W+1} = 0 \quad (8.20)$$

$$\Rightarrow E\alpha_1 = -t \left(e^{-ik\frac{A_0}{2}} \beta_1 + \beta_2 \right) \quad (8.21)$$

$$E\beta_1 = -t \left(e^{+ik\frac{A_0}{2}} \alpha_1 + \alpha_2 \right) \quad (8.22)$$

$$E\alpha_W = -t \left(e^{-ik\frac{A_0}{2}} \beta_W + \beta_{W-1} \right) \quad (8.23)$$

$$E\beta_W = -t \left(e^{+ik\frac{A_0}{2}} \alpha_W + \alpha_{W-1} \right) \quad (8.24)$$

To solve our equations of motion let us assume the solutions of the amplitudes are of the form

$$\alpha(w) = C_1 e^{+iqw} + C_2 e^{-iqw}, \quad (8.25)$$

$$\beta(w) = C_3 e^{+iqw} + C_4 e^{-iqw} \quad (8.26)$$

with C_1 to C_4 being coefficients and q as the transverse wave number. (8.21) gives us the following relations:

$$\alpha_0 = C_1 + C_2 = 0, \quad (8.27)$$

$$\beta_0 = C_3 + C_4 = 0, \quad (8.28)$$

$$\alpha_{W+1} = C_1 e^{+iq(W+1)} + C_2 e^{-iq(W+1)} = 0, \quad (8.29)$$

$$\beta_{W+1} = C_3 e^{+iq(W+1)} + C_4 e^{-iq(W+1)} = 0. \quad (8.30)$$

Hence, we have

$$\alpha_w = C_1 \left(e^{+iqw} - e^{-iqw} \right), \quad (8.31)$$

$$\beta_w = C_3 \left(e^{+iqw} - e^{-iqw} \right). \quad (8.32)$$

Let us now insert these into our equations of motion (8.18).

$$E\alpha_w = -t \left(e^{-ik\frac{A_0}{2}} \beta_w + \beta_{w-1} + \beta_{w+1} \right) \quad (8.33)$$

$$\begin{aligned} EC_1 \left(e^{+iqw} - e^{-iqw} \right) &= -C_3 t e^{-ik\frac{A_0}{2}} \left(e^{iqw} - e^{-iqw} \right) \\ &\quad - C_3 t \left(e^{iqw} e^{-iq} - e^{-iqw} e^{iq} + e^{iqw} e^{iq} - e^{-iqw} e^{-iq} \right) \end{aligned} \quad (8.34)$$

$$EC_1 \left(e^{+iqw} - e^{-iqw} \right) = -C_3 t \left(2 \cos q + e^{-ik\frac{A_0}{2}} \right) \left(e^{iqw} - e^{-iqw} \right) \quad (8.35)$$

$$EC_1 = -C_3 t \left(2 \cos q + e^{-ik\frac{A_0}{2}} \right) \quad (8.36)$$

(8.19) analogously yields

$$EC_3 = -C_1 t \left(2 \cos q + e^{+ik\frac{A_0}{2}} \right). \quad (8.37)$$

Solving (8.37) for C_3 and inserting it into (8.36) brings forth

$$E = \frac{1}{E} t^2 \left(2 \cos q + e^{+ik\frac{A_0}{2}} \right) \left(e^{-ik\frac{A_0}{2}} 2 \cos q \right), \quad (8.38)$$

$$E^2 = t^2 \left(1 + 4 \cos^2 q + (e^{+ik\frac{A_0}{2}} + e^{-ik\frac{A_0}{2}}) 2 \cos q \right). \quad (8.39)$$

Then, we finally obtain the solution for the eigenenergies as

$$E = \pm t \sqrt{1 + 4 \cos^2 q + 4 \cos q \cos k \frac{A_0}{2}}. \quad (8.40)$$

In order to calculate the quantization condition for our transverse wave number q ,

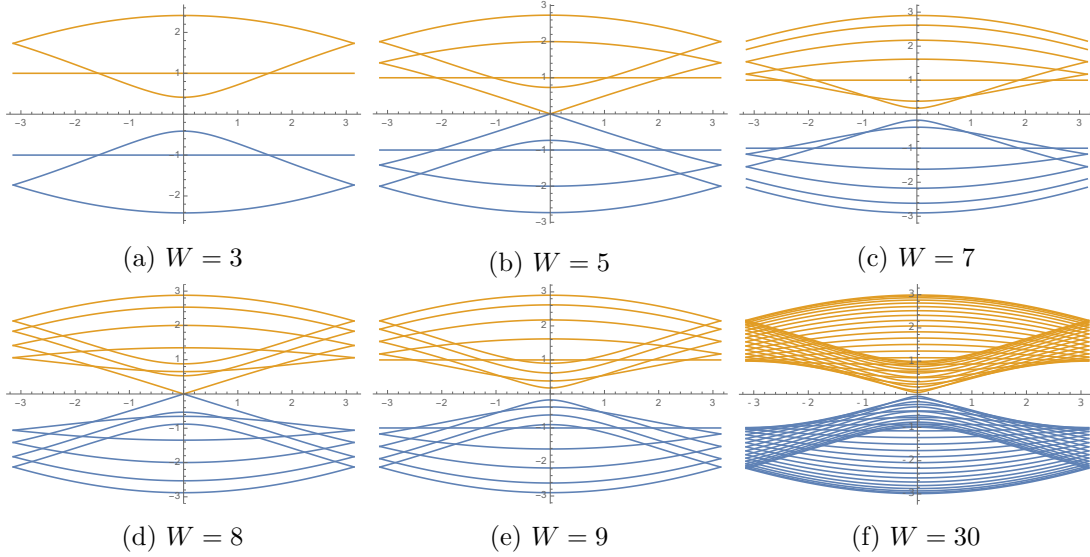


Fig. 8.3: Electronic band structure of AGNR for $t = 1$ and $A_0 = 1$. For $W = 3n + 2$ with $n \in \mathbb{N}_0$ the spectrum is semimetallic. In general, the band gap decreases with increasing W .

remember the boundary condition (8.29)

$$\begin{aligned}
 & C_1 e^{+iq(W+1)} + C_2 e^{-iq(W+1)} = 0 \\
 \Leftrightarrow & -C_1 e^{+iq(W+1)} = C_2 e^{-iq(W+1)} \\
 \Leftrightarrow & -C_1 e^{+2iq(W+1)} = C_2 \\
 \stackrel{8.27}{\Leftrightarrow} & C_2 e^{+2iq(W+1)} = C_2 \\
 \Rightarrow & 2q(W+1) = 2\pi \\
 \Rightarrow & q = \pi \frac{\nu}{W+1}, \quad \nu = 1, 2, 3, \dots, N
 \end{aligned} \tag{8.41}$$

Upon comparing the spectra of AGNR of various widths W , we learn that the spectrum is semimetallic for AGNR that fulfill

$$W = 3n + 2 \quad \text{with} \quad n \in \mathbb{N}_0 \tag{8.42}$$

and semiconducting for other, small AGNR.

In the limit of $W \rightarrow \infty$, we obtain the semimetal spectrum of an ordinary sheet of graphene.

8.3 DFT calculation for AGNR

Let us now compare the tight-binding energy spectrum (see Fig. 8.3) with the results from the DFT calculations.

In order to simulate a one-dimensional system, we spaced the GNR with about 30\AA between the y -layers and 15\AA between the z -layers, thereby eliminating interaction between them and obtaining the spectrum of an effective one-dimensional system.

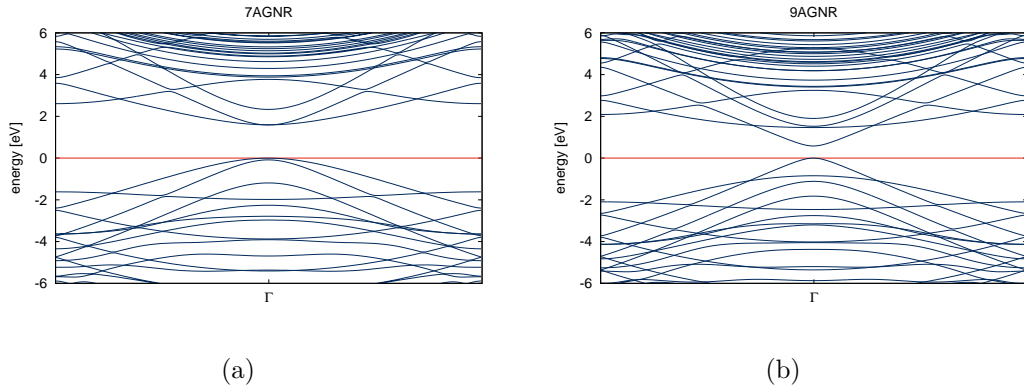


Fig. 8.4: Results of the DFT calculations for a 7AGNR (a) and a 9AGNR (9). Due to the small band gap both structures classify as semiconductors, which meets our expectations from the tight-binding calculations (see Fig. 8.3).

The density of the k -mesh has been progressively increased to 10000 points for the 7AGNR and to 5000 points for the 9AGNR, which has been reduced to 14400 and 800 k -points by WIEN2k respectively, due to the symmetries of the systems. The accuracy of energy and charge convergence has been raised to 0.0001Ry. The final energy stays nearly constant for all calculations though, so already for a loose mesh, a good convergence can be obtained.

The point $k = 0$ has been named Γ and the x -range of the plots has been chosen such that it extends to the boundaries of the respective unit cell.

Although the DFT and the tight-binding spectra show obvious deviations, we can find qualitative agreement between them. We have to keep in mind that for the tight-binding calculations only the nearest-neighbor interactions have been considered and the on-site energies at the boundaries of the ribbons, which arise due to the hydrogen saturation, have been neglected.

On the other hand, DFT tends to underestimate the band gap of a system, because of the derivative discontinuity in the exchange-correlation potential V_{xc}^σ , as discussed by means of (4.23). Additionally, there is spurious self-interaction between the states in the occupied bands, which delocalizes them and forces them up in energy.

Whether the width W fulfills (8.42), has no effect whatsoever on the spectra. They remain semiconductors for all small widths W [53]. This is probably due to the negligence of the on-site energies in the tight-binding calculations.

Examining the orbital character of the band structure of 7AGNR in Fig. 8.5, we confirm a statement of [53], where it is argued that if a mirror plane in the structure is present, the orbitals in each band do not mix. Just as expected, the bands close to the Fermi level have *out-of-plane* orbital character. These p_z -orbitals form π -bonds.

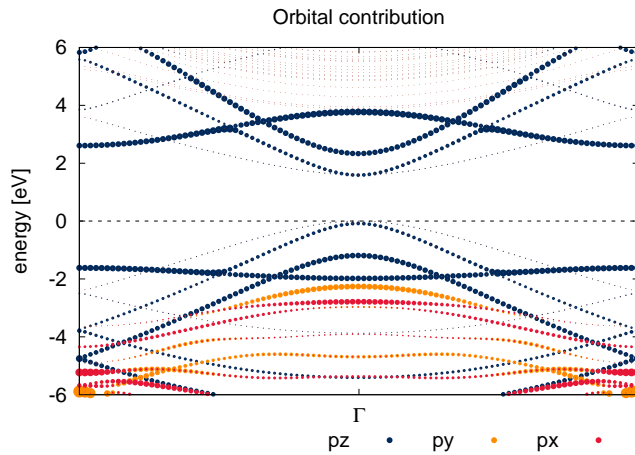


Fig. 8.5: Band structure of the 7AGNR. The thickness of the bands corresponds to orbital contribution to the band of atom B_5 (see Fig. 8.2). The different colors correspond to the different orbital types px , py and pz .

8.4 AGNR composites

Considering composite AGNR that consist of AGNR of different width, we can introduce topological defects without actually introducing impurities in our system. If the components of this composite structure have different \mathbb{Z}_2 invariants, there will be edge states, or rather interface states, that couple to each other. Through this coupling we should see new bands that are topologically induced. An AGNR of a fixed width W produces a quasi-1D

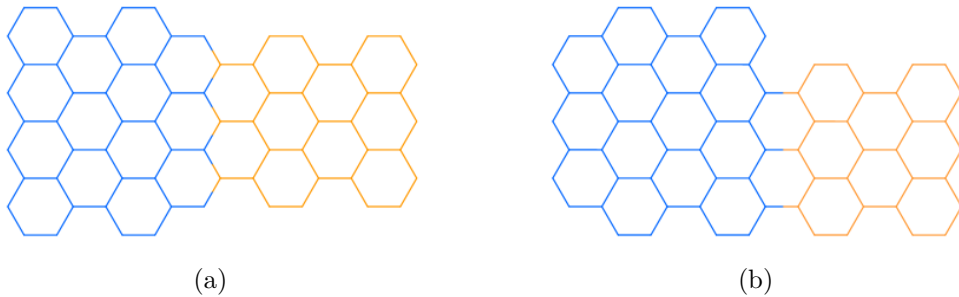


Fig. 8.6: *smooth* (a) and *abrupt coupling* (b) of 7 and 9AGNR

lattice that consists of alternating blocks of $\lfloor \frac{W}{2} \rfloor$ and $\lfloor \frac{W}{2} \rfloor - 1$ hexagons (see Fig. 8.1a). Connecting two AGNR which differ in their width by two, one can basically choose two different ways of joining the lattices.

In Fig. 8.6a the two AGNR are combined in a way such that the more narrow rows meet each other. This coupling will be referred to as *smooth coupling*, while in Fig. 8.6b the $\lfloor \frac{W}{2} \rfloor$ and the $\lfloor \frac{W}{2} \rfloor - 1$ row are coupled, which will be called *abrupt coupling*.

Since the structure proposed in [6] is too big to be calculated with our means, let us turn our attention to smaller, more manageable structures.

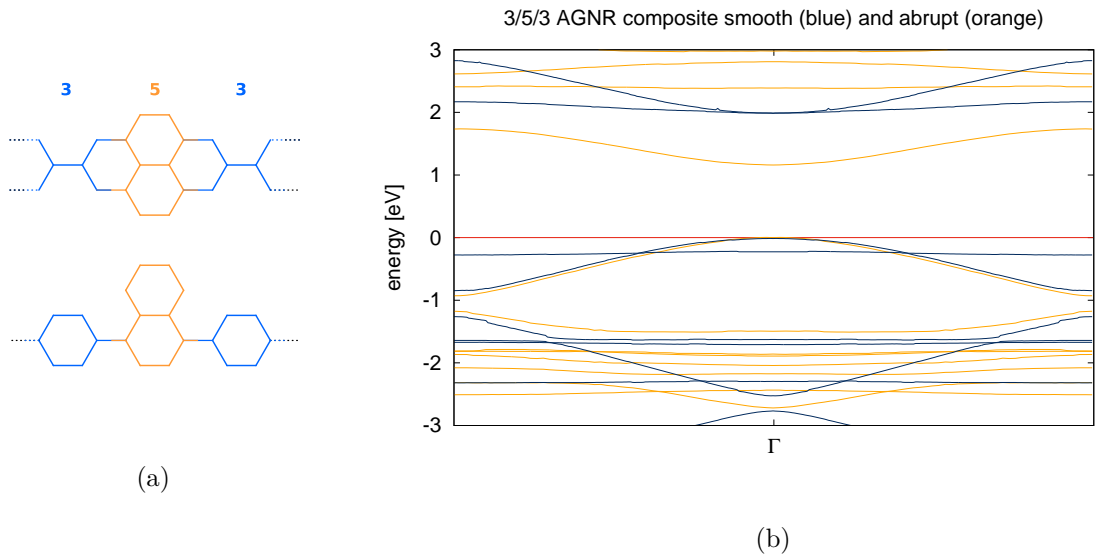


Fig. 8.7: (a) two 3/5/3 AGNR composites. The upper structure has been joined smoothly, the lower abruptly; (b) band structures resulting from DFT of the two systems given in (a). The bands corresponding to the abruptly coupled ribbon are given in orange, the others in blue. Only the components of the abruptly joined GNR have different values for the \mathbb{Z}_2 invariant.

8.4.1 3/5/3 AGNR composites

As the computational expense scales exponentially with the size of the unit cell, consider AGNR composites that consist of 3 and 5AGNR. Consulting our classification scheme for the \mathbb{Z}_2 invariant of AGNR (see Fig. 6.2), we come to the conclusion that only the abruptly coupled structure features components of a distinct topological phase. In Fig. 8.7b the DFT results for the smoothly and the abruptly joined AGNR are given. The bands of the topological composite are orange.

For both systems the electronic structure looks quite similar: The valence bands sit on top of each other and the conduction band of the abrupt structure seems to appear in the smoothly joined ribbon too, just shifted up about 1eV. At first glance, it does not look as if completely new bands appear. Notice though that the smooth composite exhibits a flat band, just below the Fermi level.

In chapter 7 it was demonstrated that the bands, which are a consequence of the coupling of the interface states, are expected to disperse like the bands in the SSH model. Hence, we expect orange bands close to the Fermi level of the form

$$E_{SSH} = \sqrt{t_1^2 + t_2^2 + 2t_1t_2 \cos k}. \quad (8.43)$$

If any of these bands resulted from such a topology, the contribution to them from the atoms sitting at the interfaces should be large compared to the other atoms. Thus, we

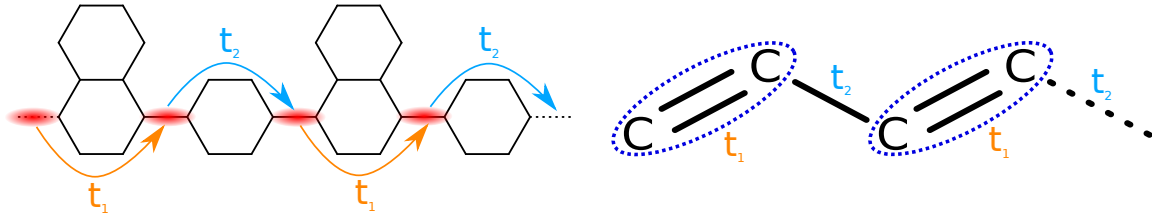


Fig. 8.8: AGNR composite and dimer chain with effective hopping t_1 and t_2 . The localized interface states between the different components of the AGNR composite correspond to the sites of the dimer chain in the SSH model. Instead of hopping along either a single or a double bond, the different components of the composite are being hopped over.

divided the atoms contained in the unit cell of the abruptly joined 3/5/3 composite into interface and non-interface atoms (see Fig. 8.9) and its band structure is given again in Fig. 8.10. Now, the thickness of the bands corresponds to the contribution of the respective group of atoms. The only bands that are in line to be of topological nature are those that are bent towards the Fermi level and cross the y -axis at approximately 2 and -1 eV respectively. In the lower plot of Fig. 8.10, the weights have been averaged with respect to the number of atoms belonging to either the interface or non-interface group. We observe that the interface atoms mainly contribute to the bands close to the Fermi level and that in average their weight exceeds the contribution of the non-interface atoms approaching this region.

As the interface states are not fully localized and should extend a certain amount into the components adjacent to the respective interface, this favors the interpretation of [6]. The parameters of the SSH dispersion (8.43) have been adjusted to fit the bands in question and have been plotted in Fig. 8.10 as well.

To match them properly, a shift of 0.55eV is necessary and the hopping amplitudes have been chosen such that $t_1 = \pm 0.38$ and $t_2 = \mp 0.96$, which yields a gap of $\Delta t = 1.34$ eV.

The authors of [6] argue that due to the smaller intrinsic band gap of the wider structure (see Fig. 8.3), the interface state's wave function decays more slowly, thus allowing it to extend further into the wider structure (here the 5AGNR). This would generate a bigger overlap compared to the overlap that corresponds to hopping over the more narrow structure, which finally results in $t_1 \neq t_2$.

Fig. 8.11 illustrates how each carbon atom contributes to the band structure and which orbitals do so. As expected, the bands are formed by out-of-plane p-orbitals.

The only contribution from in-plane orbitals that we can see in the chosen energy window comes from atom C4 and C6. The hydrogen atoms that saturate these two carbon atoms sit very close to each other (0.63Å) and the flat bands are probably a result of their immediate proximity.

The p_x - and p_y -orbitals form bonding and anti-bonding pairs which result in bands that are far away from the Fermi edge.

Referring to Fig. 8.10, we argued that mainly the interface atoms contribute to the conductance and valence band. Fig. 8.11 reveals though that atom C3 adds a significant share to these bands, although it is the atom with the largest distance to the interfaces. In analogy to the dimer chain, we expect a contribution that decays exponentially with the

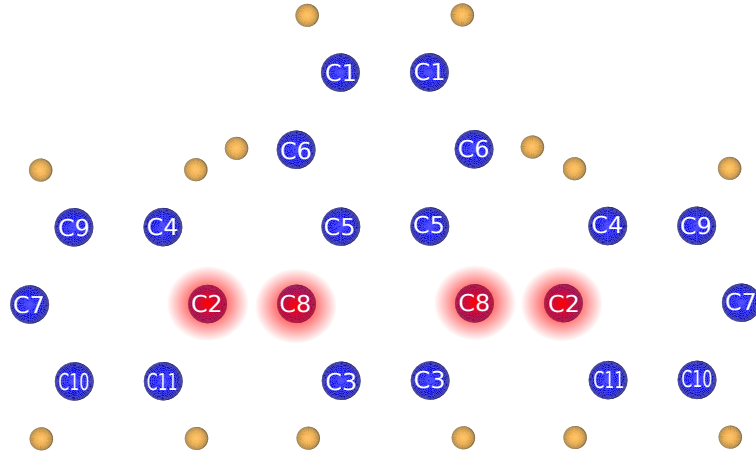


Fig. 8.9: Unit cell of the abruptly joined 3/5/3 AGNR composite. The interface atoms are marked in red and the hydrogen atoms are given in orange.

distance to the interfaces. Also, we expect carbon atoms that sit in the same component of the AGNR composite and are equally far away from an interface atom, e.g. atom C3 and C5, to contribute roughly the same weight, which is clearly not the case. The data rather implies that the position of the respective atom in transverse direction determines its contribution; if there is a trend to be found at all.

It should be mentioned that sinusoidally dispersing bands like ours are not exclusively inherent to a topological, SSH-like model. Imagine any two distinct structures which are not connected with each other. Naturally, we expect non-dispersive energy levels. Linking these structures perturbatively by slowly increasing the value of some hopping parameters t and t' would introduce dispersion similar to the SSH dispersion. Even the shift of the bands can be accounted for by considering an on-site energy.

Thus, an understanding of the electronic properties of AGNR composites can be gained easily, without considering the local topology of these structures at all.

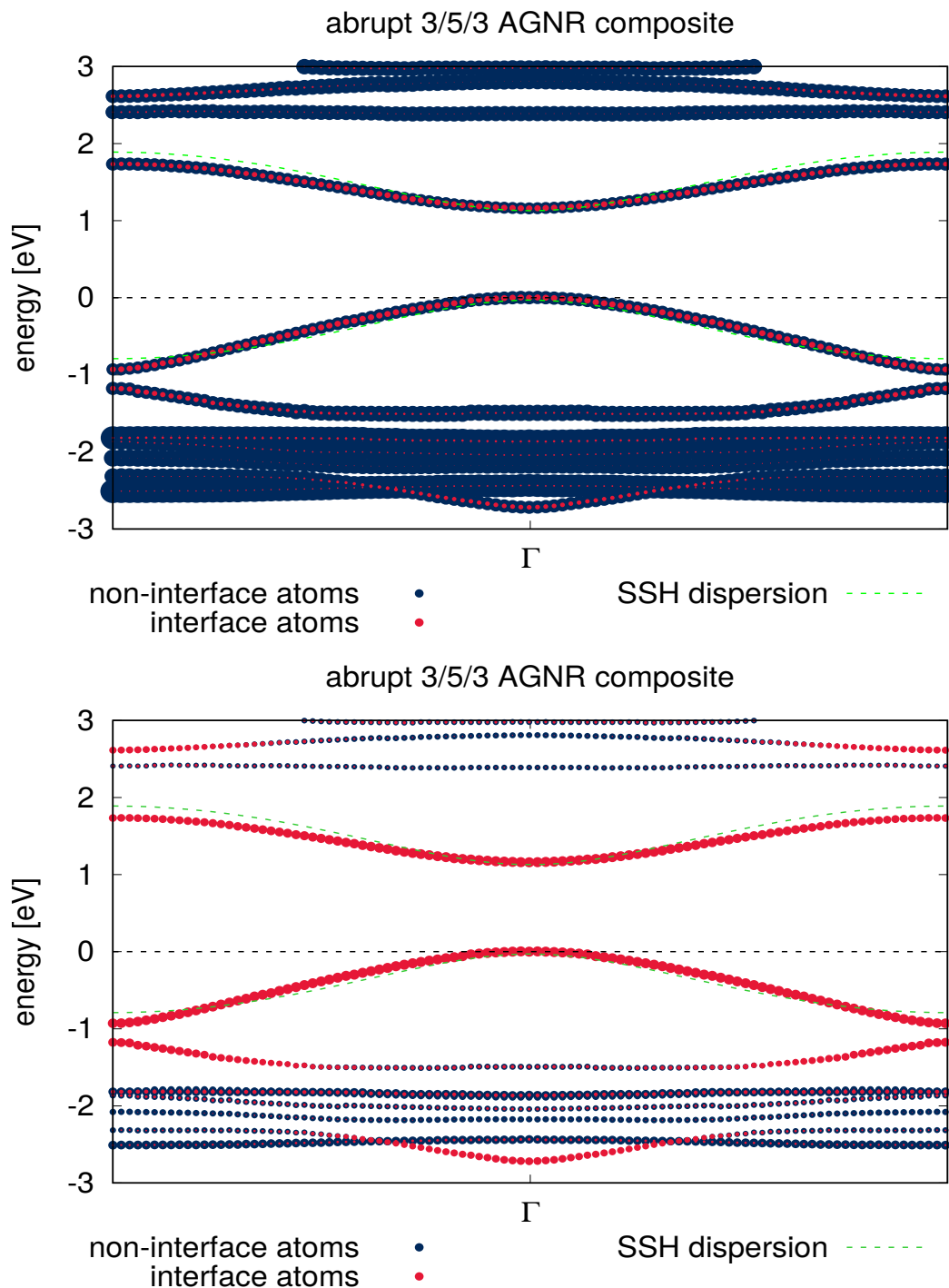


Fig. 8.10: The radii of the points assembling the graphs depend on the contribution of the chosen atoms to the bands. The contribution of the interface atoms, which are marked in red (see Fig. 8.9), is compared to the contribution of the other carbon atoms. The upper plot depicts the total weights, while the lower one is averaged with respect to the number of carbon atoms.

(8.43) with $t_1 = \pm 0.38$, $t_2 = \mp 0.96$ and an overall shift of 0.55eV yields the green, dashed line.

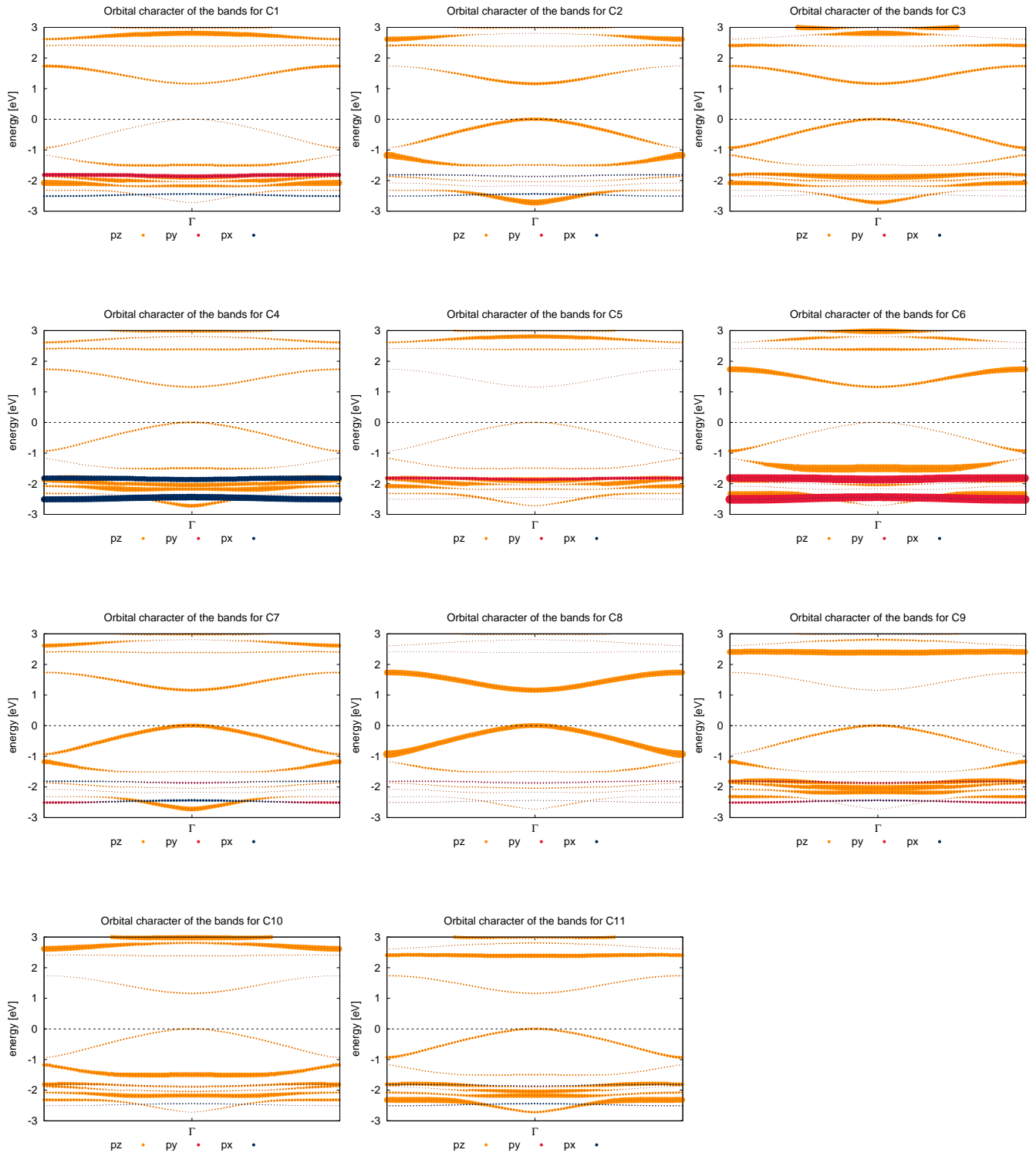


Fig. 8.11: The contribution to the bands of the p-orbitals of each carbon atom from the abruptly joined 3/5/3 AGNR composite. Different colors correspond to different orbital characters and the carbon atoms are labeled according to Fig. 8.9. Atoms C2, C3, C7 and C8 mainly contribute to the conduction and valence band. For C4 and C6 flat, in-plane bands appear.

9 Discussion and Outlook

The results presented throughout this thesis were not able to convince us that the interpretation of [6] is valid. Although the composition of structures consisting of two AGNR of different width has a notable impact on the band structure, but it is not clear why this should necessarily be a topological phenomenon, as similar dispersive properties can be obtained without employing the framework of topological band theory.

The carbon atoms of the abruptly joined 3/5/3 structure (see Fig. 8.9) sitting at the interfaces of the composite's components mainly contribute to the conductance and valence band, which are the bands in line to be of topological nature. Nevertheless, atoms that are far away from these interfaces add a significant contribution too.

Comparing the 3/5/3 AGNR composite that is coupled such that its components carry different values for their \mathbb{Z}_2 invariant with the non-topological joined structure, we find that in fact both exhibit bands that can be modeled using the SSH dispersion (see Fig. 8.7b), just with different hopping amplitudes t_1 and t_2 and a larger gap for the smoothly joined ribbons.

Furthermore, it is not clear why the decay of the localized wave functions at interfaces should depend on the intrinsic band structure of the components and why, if that is the case, small differences in band gap result in significant differences in overlap amplitude Δt .

A couple of points remain to be investigated:

- How do the hopping amplitudes t_1 and t_2 react to topology-conserving modifications like changing the length of the components within the unit cell. As the distance between the interfaces increases, the overlap of the localized wavefunctions should decrease. Can the values of t_1 and t_2 be quantified by ab-initio calculations that match the results from the fit?
- Which atoms contribute mainly to the bands with SSH-like dispersion in the non-topological AGNR composites and are those different atoms as for the structure containing topologically distinct components?
- Does one arrive at the fully dimerized limits of the SSH model by increasing the distance between interfaces and thus reducing either t_1 or t_2 ?
- Can the overlap be tuned to $t_1 = t_2$, such that the SSH-like bands touch (see Fig. 7.2c)?
- Do we find edge states at the boundaries of the structure that match the global bulk-boundary correspondence of the SSH model?

Leaving aside the fact that the interpretation given in [6] does not persuade us, it is certainly desirable to construct GNR which have a fine-tunable, electronic topology. This would not only allow to use them as precise semiconducting nanoelectronic parts, but

it is also predicted in [5] that they can be used to create antiferromagnetic Heisenberg spin chains with stable spin centers at the internal interfaces. It is suspected that these spin chains are able to host Majorana fermion states if brought into close proximity of a superconductor [54].

In conclusion, GNR are fascinating systems that bring some of the most recent fields of study in physics together. They are a promising candidate to come into use in nanoelectronic devices and will further expand our knowledge of electronic topology by challenging our understanding and forcing scientists to come up with new theories and experiments.

Acknowledgements

I want to thank my family for supporting me and making my studies possible, and Anthea and my friends (especially Hardi) for making them even enjoyable.

The group of Prof. Valentí welcomed me very heartily and besides having a lot of fun together, I always felt as if I had my own team of experts. Everyone was very helpful and I never got the feeling I annoyed anyone despite me incessantly asking about all sorts of things, whether it was physics, programming or other matters.

Special thanks to Ying, Steven, Kira, Benjamin and David who I felt spent the most time helping me.

I also want to give thanks to Anand, whom I already miss dearly and who always made time for discussing with me (besides giving an awesome lecture).

Next, let me say thank you to Mathieu for his good advice and pleasant company, and to Hendrik for providing all of us with coffee.

Lastly, thanks to Prof. Roser Valentí for helping and encouraging me, and having me in her group as the *lowest bound*.

Bibliography

- [1] J. Gray, “Did poincaré say “set theory is a disease”?”, *The Mathematical Intelligencer*, vol. 13, pp. 19–22, Dec 1991.
- [2] “The nobel prize in physics 2016.” The Royal Swedish Academy of Sciences, 2016.
- [3] D. J. Thouless, M. Kohmoto, M. P. Nightingale, and M. den Nijs, “Quantized hall conductance in a two-dimensional periodic potential,” *Phys. Rev. Lett.*, vol. 49, pp. 405–408, Aug 1982.
- [4] N. Heinsdorf, “Hall conductance as a topological invariant,” 2018.
- [5] T. Cao, F. Zhao, and S. G. Louie, “Topological phases in graphene nanoribbons: Junction states, spin centers, and quantum spin chains,” *Phys. Rev. Lett.*, vol. 119, p. 076401, Aug 2017.
- [6] D. J. Rizzo, G. Veber, T. Cao, C. Bronner, T. Chen, F. Zhao, H. Rodriguez, S. G. L. M. F. Crommie, and F. R. Fischer, “Topological Band Engineering of Graphene Nanoribbons,” *ArXiv e-prints*, May 2018.
- [7] M. Berry, “Quantal phase factors accompanying adiabatic changes,” *Proceedings of the Royal Society of London A: Mathematical, Physical and Engineering Sciences*, vol. 392, no. 1802, pp. 45–57, 1984.
- [8] M. Born and V. Fock, “Beweis des Adiabatenatzes,” *Zeitschrift für Physik*, vol. 51, pp. 165–180, Mar. 1928.
- [9] S. shen Chern, “Characteristic classes of hermitian manifolds,” *Annals of Mathematics*, vol. 47, no. 1, pp. 85–121, 1946.
- [10] K. von Klitzing, “The quantized hall effect,” *Rev. Mod. Phys.*, vol. 58, pp. 519–531, Jul 1986.
- [11] E. H. Hall, “On a new action of the magnet on electric currents,” *American Journal of Mathematics*, vol. 2, no. 3, pp. 287–292, 1879.
- [12] P. Drude, “Zur Elektronentheorie der Metalle,” *Annalen der Physik*, vol. 306, pp. 566–613, 1900.
- [13] L. Landau, “Diamagnetismus der Metalle,” *Zeitschrift für Physik*, vol. 64, pp. 629–637, Sep 1930.
- [14] R. Kubo, “Statistical-mechanical theory of irreversible processes. i. general theory and simple applications to magnetic and conduction problems,” *Journal of the Physical Society of Japan*, vol. 12, no. 6, pp. 570–586, 1957.

- [15] P. Hohenberg and W. Kohn, “Inhomogeneous electron gas,” *Phys. Rev.*, vol. 136, pp. B864–B871, Nov 1964.
- [16] M. Levy, “Universal variational functionals of electron densities, first-order density matrices, and natural spin-orbitals and solution of the v -representability problem,” *Proceedings of the National Academy of Sciences*, vol. 76, no. 12, pp. 6062–6065, 1979.
- [17] W. Kohn and L. J. Sham, “Self-consistent equations including exchange and correlation effects,” *Phys. Rev.*, vol. 140, pp. A1133–A1138, Nov 1965.
- [18] J. P. Perdew, K. Burke, and M. Ernzerhof, “Generalized gradient approximation made simple,” *Phys. Rev. Lett.*, vol. 77, pp. 3865–3868, Oct 1996.
- [19] J. P. Perdew and Y. Wang, “Accurate and simple analytic representation of the electron-gas correlation energy,” *Phys. Rev. B*, vol. 45, pp. 13244–13249, Jun 1992.
- [20] E. H. Lieb and S. Oxford, “Improved lower bound on the indirect coulomb energy,” *International Journal of Quantum Chemistry*, vol. 19, no. 3, pp. 427–439, 1981.
- [21] E. Sjöstedt, L. Nordström, and D. Singh, “An alternative way of linearizing the augmented plane-wave method,” *Solid State Communications*, vol. 114, no. 1, pp. 15 – 20, 2000.
- [22] J. K. Asbóth, L. Oroszlány, and A. Pályi, “A Short Course on Topological Insulators: Band-structure topology and edge states in one and two dimensions,” *ArXiv e-prints*, Sept. 2015.
- [23] B. A. Bernevig and T. L. Hughes, *Topological Insulators and Topological Superconductors*. Princeton University Press, 2013.
- [24] H. P. Dahal, Z.-X. Hu, N. A. Sinitsyn, K. Yang, and A. V. Balatsky, “Edge states in a honeycomb lattice: Effects of anisotropic hopping and mixed edges,” *Phys. Rev. B*, vol. 81, p. 155406, Apr 2010.
- [25] E. Engel and R. M. Dreizler, *Density Functional Theory An Advanced Course*. Springer, 2011.
- [26] M. Fruchart and D. Carpentier, “An introduction to topological insulators,” *Comptes Rendus Physique*, vol. 14, no. 9, pp. 779 – 815, 2013. Topological insulators / Isolants topologiques.
- [27] L. Fu, “Topological crystalline insulators,” *Phys. Rev. Lett.*, vol. 106, p. 106802, Mar 2011.
- [28] L. Fu and C. L. Kane, “Topological insulators with inversion symmetry,” *Phys. Rev. B*, vol. 76, p. 045302, Jul 2007.
- [29] L. Fu and C. L. Kane, “Time reversal polarization and a Z_2 adiabatic spin pump,” *Phys. Rev. B*, vol. 74, p. 195312, Nov 2006.

- [30] F. D. M. Haldane, “Model for a quantum hall effect without landau levels: Condensed-matter realization of the "parity anomaly",” *Phys. Rev. Lett.*, vol. 61, pp. 2015–2018, Oct 1988.
- [31] M. Z. Hasan and C. L. Kane, “Colloquium: Topological insulators,” *Rev. Mod. Phys.*, vol. 82, pp. 3045–3067, Nov 2010.
- [32] K.-I. Imura, S. Mao, A. Yamakage, and Y. Kuramoto, “Flat edge modes of graphene and of z2 topological insulator,” *Nanoscale Research Letters*, vol. 6, p. 358, Apr 2011.
- [33] G. Jotzu, M. Messer, R. Desbuquois, M. Lebrat, T. Uehlinger, D. Greif, and T. Esslinger, “Experimental realization of the topological haldane model with ultracold fermions,” *Nature*, vol. 515, pp. 237 EP –, Nov 2014.
- [34] C. L. Kane and E. J. Mele, “ Z_2 topological order and the quantum spin hall effect,” *Phys. Rev. Lett.*, vol. 95, p. 146802, Sep 2005.
- [35] C. L. Kane and E. J. Mele, “Quantum spin hall effect in graphene,” *Phys. Rev. Lett.*, vol. 95, p. 226801, Nov 2005.
- [36] M. Kohmoto, “Topological invariant and the quantization of the hall conductance,” *Annals of Physics*, vol. 160, no. 2, pp. 343 – 354, 1985.
- [37] R. B. Laughlin, “Quantized hall conductivity in two dimensions,” *Phys. Rev. B*, vol. 23, pp. 5632–5633, May 1981.
- [38] R. M. Martin, *Electronic Structure: Basic Theory and Practical Methods*. Cambridge University Press, 2004.
- [39] J. E. Moore and L. Balents, “Topological invariants of time-reversal-invariant band structures,” *Phys. Rev. B*, vol. 75, p. 121306, Mar 2007.
- [40] C.-H. Park and N. Marzari, “Berry phase and pseudospin winding number in bilayer graphene,” *Phys. Rev. B*, vol. 84, p. 205440, Nov 2011.
- [41] S. Rachel, “Interacting Topological Insulators: a review,” *ArXiv e-prints*, Apr. 2018.
- [42] R. Roy, “Topological phases and the quantum spin hall effect in three dimensions,” *Phys. Rev. B*, vol. 79, p. 195322, May 2009.
- [43] A. P. Schnyder, S. Ryu, A. Furusaki, and A. W. W. Ludwig, “Classification of topological insulators and superconductors in three spatial dimensions,” *Phys. Rev. B*, vol. 78, p. 195125, Nov 2008.
- [44] A. Sharma, “Lecture notes on modern trends in topological condensed matter.” Goethe Universität Frankfurt, 2018.
- [45] K. Sun, “Condensed matter physics 620.” University of Michigan, 2012.
- [46] D. Tong, “Lectures on the Quantum Hall Effect,” *ArXiv e-prints*, June 2016.
- [47] R. Valenti, “Theorie zu Magnetismus, Supraleitung und Elektronische Korrelation an Festkörpern.” Goethe Universität Frankfurt, 2018.

- [48] K. Wakabayashi, K. ichi Sasaki, T. Nakanishi, and T. Enoki, “Electronic states of graphene nanoribbons and analytical solutions,” *Science and Technology of Advanced Materials*, vol. 11, no. 5, p. 054504, 2010.
- [49] J. Zak, “Berry’s phase for energy bands in solids,” *Phys. Rev. Lett.*, vol. 62, pp. 2747–2750, Jun 1989.
- [50] “The nobel prize in physics 2010.” The Royal Swedish Academy of Sciences, 2010.
- [51] R. E. Peierls, *Quantum Theory of Solids*. Oxford University Press, 2001.
- [52] P. Delplace, D. Ullmo, and G. Montambaux, “Zak phase and the existence of edge states in graphene,” *Phys. Rev. B*, vol. 84, p. 195452, Nov 2011.
- [53] Dubois, S. M.-M., Zanolli, Z., Declerck, X., and Charlier, J.-C., “Electronic properties and quantum transport in graphene-based nanostructures,” *Eur. Phys. J. B*, vol. 72, no. 1, pp. 1–24, 2009.
- [54] A. Heimes, P. Kotetes, and G. Schön, “Majorana fermions from shiba states in an antiferromagnetic chain on top of a superconductor,” *Phys. Rev. B*, vol. 90, p. 060507, Aug 2014.